Osaka University Knowledge Archive

Title	A Subject-Specific Correction of Four-Dimensional Flow Magnetic Resonance Images for Cerebrospinal Fluid Flow Measurements
Author(s)	Yavuz Ilik, Selin
Citation	大阪大学, 2022, 博士論文
Version Type	VoR
URL	https://doi.org/10.18910/89648
rights	
Note	

Osaka University Knowledge Archive : OUKA

https://ir.library.osaka-u.ac.jp/

Osaka University

A Subject-Specific Correction of Four-Dimensional Flow Magnetic Resonance Images for Cerebrospinal Fluid Flow Measurements

Selin Yavuz Ilik

September 2022

A Subject-Specific Correction of Four-Dimensional Flow Magnetic Resonance Images for Cerebrospinal Fluid Flow Measurements

A dissertation submitted to

THE GRADUATE SCHOOL OF ENGINEERING SCIENCE

OSAKA UNIVERSITY

in partial fulfillment of the requirements for the degree of

DOCTOR OF PHILOSOPHY IN ENGINEERING

Selin Yavuz Ilik

September 2022

ABSTRACT

Flow magnetic resonance imaging (Flow MRI) is a non-invasive method that is capable of visualizing in-vivo human body fluid flow velocities. The four-dimensional (4D) flow MRI supplies a time series of velocity components in three directions (superior-inferior, anterior-posterior, left-right) during the cardiac cycle, and enables flow visualization, recording, and measurement of not only the blood flow in the cardiovascular system but also cerebrospinal fluid (CSF) flow in the neurological system. However, there is still no consensus about the usage of 4D flow MRI for analyzing slow flows like CSF, because of non-negligible phase-offset errors caused by its acquisition principles. Since the 4D flow MRI is a unique tool to understand CSF pathophysiology for managing diseases, this study considers an automated approach for the correction of phase offset errors in the CSF flow velocity map. Furthermore, objective methods were suggested for analyzing CSF flow by 4D flow MRI after correction of phase offset errors.

In Chapter 2, 4D flow MRI basics and limitations are explained. The MRI is based on nuclear magnetic resonance (NMR) of the nucleus, and in flow MRI magnetic field gradients are used for calculating the velocity of mobile hydrogen nuclei. Phase-contrast MRI is the most popular flow MRI which is acquired by using bipolar gradients for eliminating magnetic field inhomogeneities on nuclei. The range of the velocity is determined by the strength of the bipolar gradients. Measuring slow flows requires low-velocity encoding which needs large bipolar gradients. However, these large gradients cause unexpected electromagnetic induction resulting in nonnegligible phase offset errors. Besides, the low-spatiotemporal resolution also leads to errors like partial volume artifacts.

In Chapter 3, an automated correction method for the phase offset errors of 4D flow MRI was presented. Since the phase offset errors were assumed to be constant in time and

smoothly distributed spatially in previous existing studies, the spatial distribution of the phase offset errors was modeled as the second-degree polynomial function using robust regression analysis. Flow velocity maps were corrected by the estimated phase-offset errors by robust regression analysis. The method was applied to the CSF flow maps obtained by 9 idiopathic normal-pressure hydrocephalus (iNPH) patients and 9 healthy subjects' 4D flow MRI data. The residual standard errors between the original data and the estimated phase-offset errors were analyzed for the evaluation of estimation consistency and found under 1.7 mm/s for each case. This chapter provides an approach to the correction of phase offset errors for enabling more robust and advanced CSF studies.

In Chapter 4, flow rates in aqueduct cerebri were evaluated from the CSF velocity maps corrected in Chapter 3. The aqueduct cerebri was segmented and aliasing artifacts and partial volume artifacts were corrected before calculations. For these processes, semi-automated and automated approaches were suggested with aim of creating an objective environment for the analysis of CSF flow parameters. Flow rates were calculated for the analyzing CSF flow in this study, and significant differences were found at peak diastolic flow rates between iNPH patients and healthy cases. ($p=0.02$, Mann-Whitney's U test). Additionally, the mean aqueduct cerebri area at the axial plane was found significantly different ($p=0.01$, Mann-Whitney's U test).

In the final chapter, the dissertation is summarized, and future perspectives were given. This study aims to create an objective and automated image process for improving CSF studies with 4D PC-MRI. In this way, we hope future studies could build parameters for understanding CSF pathophysiology in an objective environment.

LIST OF ABBREVIATIONS

1- CSF: Cerebrospinal Fluid

2- MRI: Magnetic Resonance Imaging

3- iNPH: Idiopathic Normal Pressure Hydrocephalus

4- ISF: Interstitial Fluid

5- Flow MRI: Flow Magnetic Resonance Imaging

6- PC-MRI: Phase Contrast Magnetic Resonance Imaging

7- 2D: Two-Dimensional

8- 3D: Three-Dimensional

9- 4D: Four-Dimensional

10- 4D Flow MRI: Four-Dimensional Flow Magnetic Resonance Imaging

11- RF: Radio Frequency

12- ROI: Region of Interest

13- VOI: Volume of Interest

14- NMR: Nuclear Magnetic Resonance

15- NMRI: Nuclear Magnetic Resonance Imaging

16- FID: Free Induction Decay

Table of Contents

1. Introduction to Research ····· 1

1.1 Backgrounds ····· 1

1.2 CSF Dynamics from Past to the Recent Understandings ····· 3

1.3 Flow Magnetic Resonance Imaging ····· 7

1.4 PC-MRI Studies on Cerebrospinal Fluid Flow ····· 10

1.5 Motivations ····· 12

1.6 Research Aims ····· 13

1.7 Thesis Overview ····· 14

2. Four-Dimensional Flow MRI Principles and Limitations ····· 16

2.1 Introduction ····· 16

2.2 Nuclear Magnetic Resonance ····· 17

2.2.1 Free Induction Decay ····· 21

2.2.2 FID Interpretation: Relaxation Times ····· 23

2.3 Nuclear Magnetic Resonance Imaging ····· 25

2.4 Flow MRI Principles ····· 27

2.4.1 NMR of a Mobile Nucleus ····· 27

2.4.2 Phase-Contrast MRI Principles ····· 30

2.4.3 Velocity Encoding ····· 35

2.4.4 Four-Dimensional Flow MRI ····· 37

2.5 Four-Dimensional PC-MRI Limitations ····· 38

2.5.1 Aliasing Artifacts ····· 39

2.5.2 Partial Volume Artifacts ····· 40

2.5.3 Phase-offset Artifacts ····· 40

3. Objectified Phase Offset Error Correction in 4D PC-MRI ····· 42
3.1 Introduction ····· 42
3.2 Data Acquisition Principles and Features ····· 43
3.3 Methods ····· 45
3.3.1 Phase Offset Error Spatial Distribution Analysis ····· 45
3.3.2 Evaluation of Regression Analysis and Background Noise ····· 51
3.4 Results ····· 51
3.5 Discussion ····· 58
4. Objectified Approach to Calculation of Flow Rate in Aqueducts Cerebri ····· 60
4.1 Introduction ····· 60
4.2 Effects of ROI Selection on Flow Measurements ····· 62
4.3 Aliasing Artifacts and Partial Volume Artifacts' Effects on Flow Measurements ····· 63
4.4 Methods ····· 67
4.4.1 Semi-automated selection of VOI ····· 67
4.4.2 Anatomy-Based Automated Aliasing Correction ····· 75
4.4.3 Automated Correction of Partial Volume Artifacts and Flow Rate Calculation · 86
4.5 Results ····· 89
4.6 Discussion ····· 95
5. Summary and Future Perspectives ····· 98
6. Bibliography ····· 100
Publication List ····· 110
Acknowledgments ····· 111

1. Introduction to Research

1.1 Backgrounds

The central nervous system is composed of the brain and the spinal cord, and these structures stand for everything about human life. They are the most important parts of the human body, and consequently the most protected organs. Even blood that is carrying oxygen and all other fundamental components to the tissues does not have permission to interact directly with the brain and the spinal cord. Blood-brain barrier and blood-spinal barrier restrict the transfer of components between blood and the brain and spinal cord [1]. The cerebrospinal fluid (CSF) which is most of the extracellular fluid in the central nervous system could make interactions with the brain, the spinal cord, and the interstitial fluid directly. CSF surrounds the whole central nervous system, and it is positioned in the subarachnoid space and brain ventricles which are connected by channels and are positioned at the center of the brain. The CSF volume is acknowledged as approximately 150 mL depending on the person as 125 mL in subarachnoid space and 25 mL in ventricles [2].

CSF has many roles in the neurological system and still some features are not understood completely. The most visible function of the CSF is its mechanical function for the brain. It supports the brain and the spinal cord; reduces the brain weight nearly by 95% with buoyancy [3]. It helps protection of intracranial volume by osmoregulation, carries hormones, proteins, peptides, and nutrients, and plays a role in signal transduction between different parts of the neurological system[4]. CSF is completely renewed four times a day and is accepted like the lymphatic system of the neurologic system, and besides carrying wastes, such as toxic molecules[2,4–6]. Impairment in CSF circulation has been shown could lead to neurological diseases like Alzheimer's disease, normal pressure hydrocephalus (NPH), and autism because of the reasons like accumulation of toxic molecules (Amyloid-B, etc.) or imbalance at production-reabsorption or unknown reasons. [7,8].

Until the last century, human CSF dynamics have been a big, uncovered mystery for scientists. In vivo experiments were limited to animals and only some parameters were able to acquire from patients by invasive methods. Imaging methods were limited to anatomical analyses by magnetic resonance imaging (MRI) and computed tomography. From the past century to today, animal experiments and computational analyses created an environment for

modern CSF dynamics understanding. However, these approaches could not find a strong base because of a deficiency of real flow data. At this point, flow MRI allowed an understanding of physiological and pathological flow patterns [9,10].

The remainder of this section is organized as follows. Recent understandings of the CSF dynamics were explained in 1.2, a short introduction was made to flow MRI in section 1.3 and its usage in CSF research was mentioned in 1.4. At the end of the section, the motivations of this thesis and research aims were explained in 1.5 and 1.6 respectively. The outlines of the research were given in section 1.7.

1.2 CSF Dynamics from Past to the Recent Understandings

CSF has been known for thousands of years. Although the papers about CSF could be found even in Greek times and there are notes written by Leonardo Da Vinci, more scientific approaches to CSF were begun pursued in the last century with experimental results conducted by scientists like Cushing, Dandy, etc. [11]. They laid the foundations of the classical understanding of the CSF and the classical approach continued for long years without questioning. Based on the classical approach, the CSF is formed by the choroid plexus which is positioned on the ventricular walls. The CSF moves unidirectional to the subarachnoid

space and is absorbed by the arachnoid villus to the venous sinuses [12]. In the classical approach, the choroid plexus (Fig. 1B, C) is accepted as the only producer and regulator of the CSF. This supposition mainly was dependent on Dandy's experiments with one dog, though the same results could not be repeated [13]. However, recent experiments have shown that CSF circulation is not as basic as mentioned in the classical approach [11–13].

Some researchers reported that CSF production was not influenced by removing the choroid plexus in humans and monkeys, and animal experiments with dogs and rabbits showed that CSF production of extra-choroidal structures is unneglectable [4]. Another research was designed by placing a cannula in the aqueducts cerebri which is the channel connecting the third ventricle to the fourth ventricle, and researchers observed only one drop of CSF at the end of the cannula, and they did not observe any CSF pressure increasing when they blocked CSF way out[14,15]. In recent years, experiments and computational simulations have shown that the classical approach is questionable and far away from the truth[5,6]. However, cerebrospinal dynamics are still under debate depending on the deficiency of harmless and reproducible research methods which could be applicable to healthy humans. Recent notions are mostly accepted that CSF production is not only by the choroid plexus

but also from brain parenchyma by interstitial fluid (ISF), and absorption is not only from the arachnoid villus but also from the nerve roots and ISF [3,11–13,16].

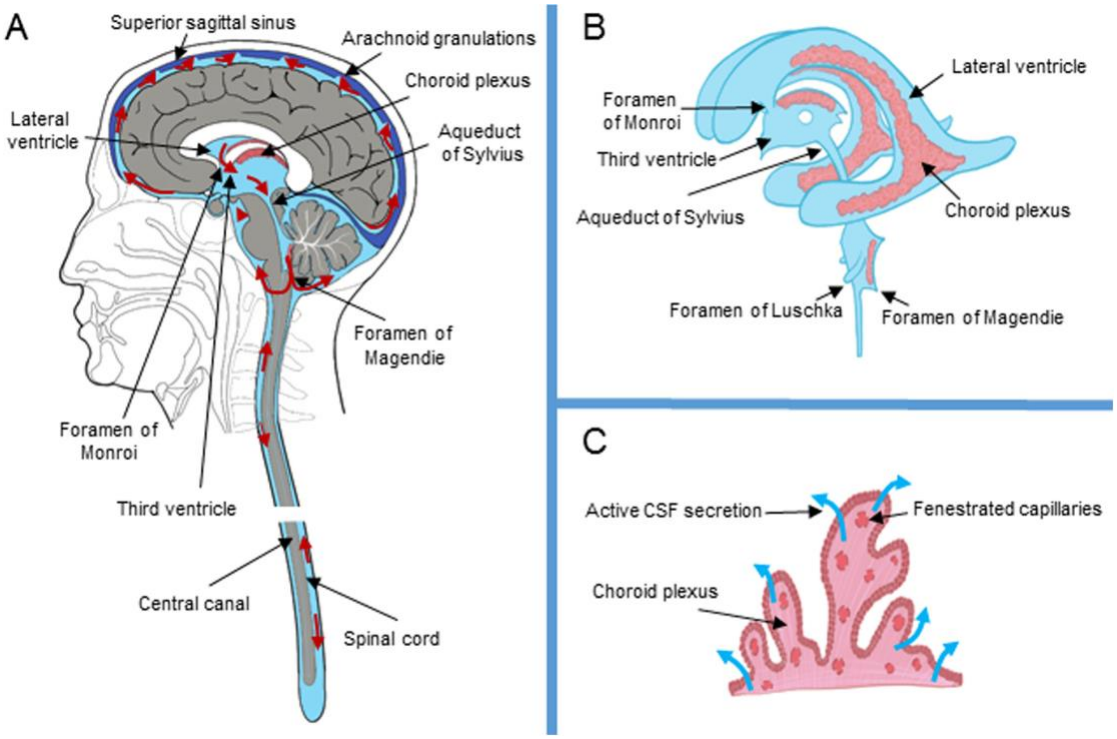

Figure 1: This figure shows the circulation and production of CSF based on the classical approach [5]. 1.A shows the anatomy of CSF which is around neurological system components and inside of ventricles. 1.B shows ventricles separately and choroid plexus placed inside them. 1.C shows CSF production by choroid plexus.

1.3 Flow Magnetic Resonance Imaging

Flow MRI is a method that is capable of measuring *in-vivo* velocity without invasive intervention [17,18]. It is used in clinical sciences for acquiring flow information of human body fluids noninvasively to discriminate physiological and pathological flow features and has taken a role as a unique and indispensable diagnostic tool in medicine. The most popular type of flow MRI is phase-contrast MRI (PC-MRI) related to its advantages compared to the other flow imaging methods.

Three-dimensional (3D) flow MRI data present magnitude (anatomical image) and velocity (phase shift) information in three different main directions: superior-inferior, anterior-posterior, and left-right (Fig.2). The acquisition of the 3D flow MRI data during the cardiac cycle constitutes four-dimensional flow MRI (4D flow MRI) [17,18].

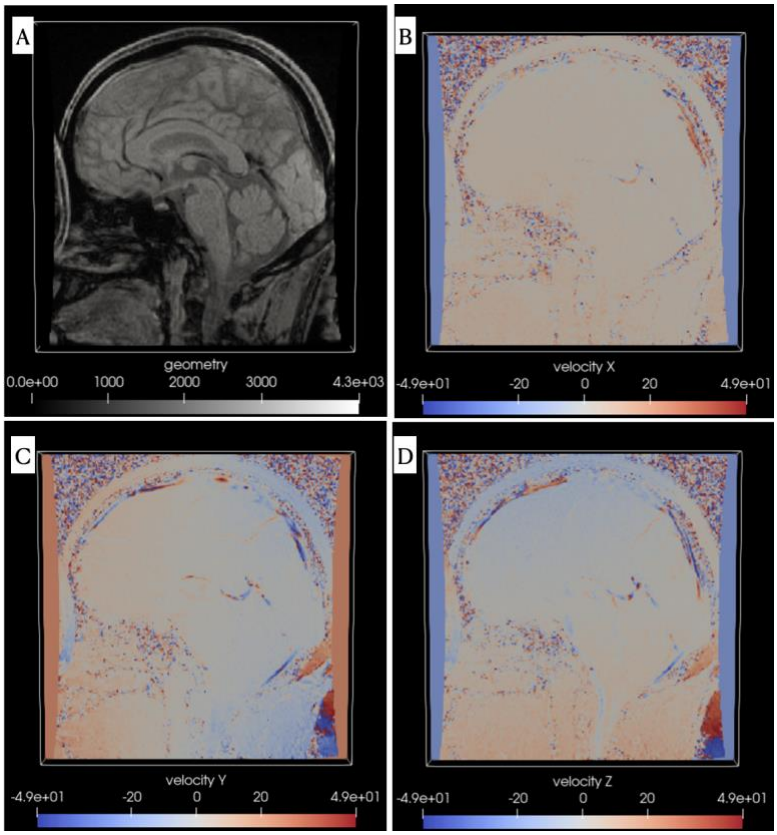

Figure 2: Sagittal plane representations of the 4D Flow MRI magnitude and velocity data. 2A shows the magnitude image obtained by phase-contrast magnetic resonance imaging and other images 2B, 2C, and 2D show velocity data respectively: left-right (velocity X), anterior-posterior (velocity Y), and superior-inferior (velocity Z) direction. For velocity data, negative and positive values declare the direction of flow, and magnitudes give velocity values. For example, the "-5" for the superior-inferior velocity map shows the voxel nuclei have 5 mm/s velocities from inferior to superior, and the "5" shows 5 mm/s velocities from superior to inferior.

Flow MRI principles depend on the calculation of the velocity of nuclei by analyzing free induction decays obtained from nuclei under magnetic field gradient. PC-MRI is obtained by neutralizing signals created by nuclei features by using a second gradient field with the same magnitude and the opposite direction and reaching signals originated by only the movement of nuclei in a gradient magnetic field. During this process, bipolar magnetic gradients are used for creating opposite gradient fields[19,20]. The applied opposite gradient fields with the same magnitudes neutralize phase shifts that are created by radio frequency (RF) pulses, and according to that, only velocity-dependent signals' acquisition is expected as a difference between phases. However, based on errors which are originated from different sources, acquired results may not correctly represent velocity information. These error sources could be machine properties, patients (motion, etc.), or based on acquisition principles themselves. In studies that are conducted on the evaluation of errors due to PC-MRI measurement techniques and limitations, it was observed that eddy-current artifacts are one of the non-negligible phase offset artifacts[20–25]. Anything which is making changes in the intensity or direction of a magnetic field can produce eddy currents and its magnitude is proportional to the rate of change in the magnetic field according to Faraday's Law. Since

PC-MRI is formed by changes in the signal phase in the magnetic gradient fields, eddy-currents creation is expected, and these currents lead to phase offset errors. Aliasing artifacts also caused to detection of incorrect velocity information. These artifacts are seen when velocity is exceeding v_{enc} (velocity encoding: the determined maximum velocity), and it leads to incorrect velocity measured.

Signal to noise ratio represents the ratio between acquired signal and background noise. This ratio shows the signal's affection degree from the errors. For the more correct results, signal to noise ratio should be high. Based on this, while PC-MRI artifacts could be compensated in high-velocity flow areas, the same magnitude artifacts would make correct signal acquisition impossible in slow-flow areas. As a result, artifacts should be removed as much as possible for the robust measurement of velocity which belongs to the slow-flow fields like CSF. PC-MRI principles and limitations will be explained in the next chapter with details.

1.4 PC-MRI Studies on Cerebrospinal Fluid Flow

The PC-MRI is used to analyze the difference between pathological and physiological CSF flow dynamics by comparing healthy cases and patients who have neurological diseases.

Researchers have tried to find markers to identify pathological conditions [26–29]. iNPH, which is a neurological disease characterized by enlarging ventricles with normal intracranial pressure and together with some clinical symptoms like cognitive impairment [30], has been the most attractive topic. Some research showed NPH patients have different flow dynamics like increased stroke volume in aqueducts cerebri[28,29,31]. However, spatiotemporal resolution limitations and low signal-to-noise ratio for the slow velocity is still critical drawback of the PC-MRI studies on CSF dynamics.

Even though 4D PC-MRI is the most promising and usable method that is capable of the visualization of CSF flow, there is no consensus in previous research about the usage of PC-MRI for CSF research [32]. The subjectivity in processing like manual correction of errors, choosing a region of interest, etc. could be shown as reasons for un-consensus. These limitations grievously obstruct studies about CSF dynamics and its interactions with surrounding brain tissue. Depending on limitations, CSF studies could not be expanded outside of aqueducts cerebri except for a couple of research with using computational fluid dynamics [9,32].

1.5 Motivations

The importance of CSF was explained in previous sections. Flow MRI is the most promising diagnosis tool which enables inspection of CSF dynamics. With the improving processing of flow MRI, quantifying CSF and understanding its circulation could be possible. In this way, the understanding of the physiopathology of diseases could be supported. The parameters which could be used for the discrimination of disease could be built. With the understanding of physiopathology, more efficient treatment options could be discovered by scientists. With clear circulation knowledge, the drug administration could be managed clearly, and bioavailability and elimination of the drugs could be estimated more precisely.

However, unfortunately, depending on its limitations, most of the possible usage areas of flow MRI could not reach their potential and a consensus could not build among scientists about its clinical usage for CSF. The motivation for this study is decreasing limitations and preparing an appropriate environment for making flow MRI reach its potential in CSF flow analysis.

1.6 Research Aims

The main aim of this research is to remove phase offset errors and reach correct velocity information automatically. Since in previous studies correction of phase offset error is generally removed manually or semi-automatically in only local regions, there is no criterion for evaluating if the data is appropriate for the study[27,28]. Besides, not automatic corrections could lead to different results obtained from the same data by different researchers. Furthermore, the lack of automated correction limits studies extent because of time limitans for each case process. Besides, not only phase-offset errors affect velocity data. Additionally, aliasing artifacts and partial volume artifacts are known as limitations that could affect results during the calculation process of parameters.

The aim of this research enabling the correction of phase offset errors automatically and remove subjectivity and decrease the time for image processing. Additionally, decreasing subjectivity in the calculation process by making automatic corrections of aliasing artifacts and partial volume artifacts is purposed.

1.7 Thesis Overview

In this chapter, CSF features were explained, and an introduction was made to flow MRI. The fundamentality of the usage of flow MRI in CSF research was pointed out. The motivations and aims of the research were mentioned.

In the second chapter, four-dimensional PC-MRI (4D PC-MRI) principles were explained in detail. After principles, the limitations of PC-MRI were defined in the light of principles.

In the third chapter, an automatic correction method for the phase offset errors was suggested and the results of the application on 18 cases' 4D PC-MRI data were presented.

In the fourth chapter diastolic-systolic flow rates of data which are processed in Chapter 3 were calculated. During the calculation, for selection of the volume of interest (VOI), correction of aliasing artifacts, and partial volume artifacts, automated and semi-automated approaches were suggested and a comparison of results between healthy cases and iNPH patients was presented.

In the final chapter, the research was summarized, and future perspectives were mentioned.

The figures in the thesis were created by using Para View (free visualization software) and Python Matplotlib package. Before visualization, Pandas, Numpy, SimpleITK, openpyxl, xlrd, and h5py packages were used during the data process. Additional libraries used in the research were explained in relating sections.

2. Four-Dimensional Flow MRI Principles and Limitations

2.1 Introduction

The first human body experiment of MRI with a volunteer person was recorded in 1977[33]. Since then, MRI made a quick entry into clinical sciences and has become one of the main diagnosis and treatment managing tools in medicine. In the following years, scientists made experiments for measuring blood flow by adjusting MRI acquisition methods differently. Only 9 years after the first experiment of MRI on the human body, blood flow imaging by cine magnetic resonance principles were announced by Nayler et al. in 1986[34].

PC-MRI is a complicated method that includes many complex processes. Some properties of PC-MRI differ based on machine features. Echo time, repetition time, velocity encoding, and a cardiac number of images are some parameters for obtaining PC-MRI images. Some of these parameters can be adjusted by the users according to patient, illness, and aim. As an instance, velocity encoding determines the measurable highest velocity value with PC-MRI. This parameter can be set depending on the velocity distribution of the measuring region, such as the heart, and brain, and can be set differently from person to person. For all these reasons, PC-MRI studies require a comprehension of its principles.

In this chapter, 4D PC-MRI principles were explained from magnetization to 4D image acquisition. At the end of the section, PC-MRI limitations were clarified based on principles.

2.2 Nuclear Magnetic Resonance

Felix Bloch discovered atomic nuclei have their magnetic nature in 1946 . Even though the nucleus does not have orbital motions like electrons, scientists built a hypothesis that nucleons also have their spins. It can be thought that the nucleus rotates around an axis that is passing at the nucleus's gravity center. This spin of the nucleus with charges brings amperian currents like electrons and creates a magnetic effect. Net nuclear spin and the magnetic effect of the nucleus are directly affected by proton and neutron numbers. Only the nucleus in which at least one nuclear particle has odd numbers has a net nuclear spin and magnetic power[33].

There are two different forces on the protons in the magnetic field: spinning, which is already what protons have, and the magnetic field. These two forces' effects produce precession of the nucleus like spinning tops in the effect of the gravitational field (Fig.3)[35].

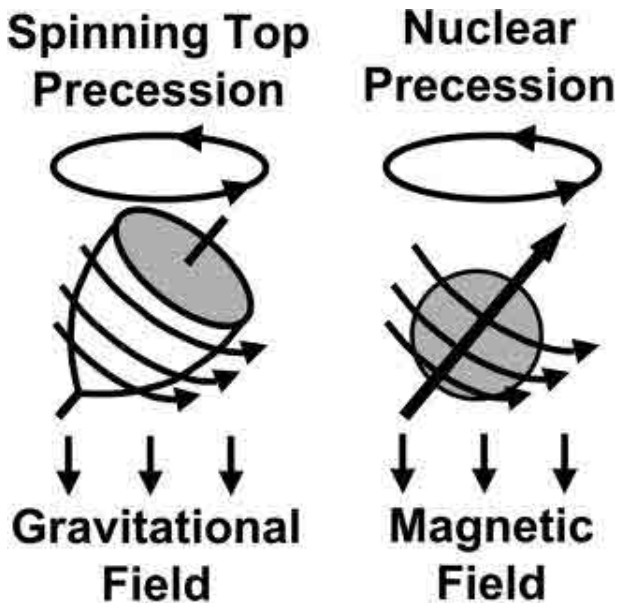

Figure 3: The schematization of the nuclear precession under magnetic field with the similitude of spinning top precession under the gravitational field[35].

The frequency of the nuclear precession (Larmor frequency) f is given by [35,36]

$$f = \frac{\gamma B}{2\pi} \tag{1}$$

where γ is the gyromagnetic ratio specific to the atomic nuclei [37] and B is the strength of the magnetic field. Based on the classical electrodynamics approach [37], the nuclear precession can be described as

$$\frac{dM}{dt} = -\gamma M \times B = -M \times \omega \tag{2}$$

where M is the sum of all nuclear magnetic moments (net nuclear magnetization) and ω is the angular frequency ($\omega = 2\pi f = \gamma B_0$)).

In the static magnetic field, protons make precession through the magnetic field axis with "zero angles", and thus precession cannot be detected[38]. Scientists proposed an approach for measuring precessions of the nucleus by applying RF energy [38] which is perpendicular to the static magnetic field and has the same frequency as the nucleus. The nucleus absorbs this energy and increased energy creates resonance at the nucleus. This process is known as nuclear magnetic resonance (NMR). After cutting RF pulses, nuclei return to their equilibrium. While nuclei return to equilibrium, nuclei lose energy that was

taken from RF pulses, and these are known as free induction decay (FID) and could be measured.

However, the measurement of only one nucleus precession is not compatible with real experiments. In the reality, signals are obtained from a macroscopic field. Bloch formulated precession features of the macroscopic field with the following equations including the calculation of polarization for each direction in the coordinate system [39]:

$$M_x = \frac{M}{(1+\delta^2)^{\frac{1}{2}}} \cos\omega t \qquad (3a)$$

$$M_y = \frac{M}{(1+\delta^2)^{\frac{1}{2}}} \sin\omega t \qquad (3b)$$

$$M_z = \frac{M}{(1+\delta^2)^{\frac{1}{2}}} \qquad (3c)$$

where x, y, and z represent three different directions of the coordinate system and $\delta = \frac{(B_0 - B^*)}{B_1}$ which represents the rate of deviation of B_0 (static magnetic field) from the B^* (magnetic field on specific coordinates of sub volume in the matter) to the half of the oscillating magnetic field ($B_1 = {}^{B_x}/_{2 * \cos \omega t}$, x : oscillating direction).

2.2.1 Free Induction Decay

Although the net nuclear magnetization is tilted by the application of RF pulses, this tilting began to decay in milliseconds after RF pulses are stopped, and the net magnetization return to equilibrium. This decay is known as free induction decay (FID). During the RF application process, the net magnetization of the nucleus changes from the parallel to the static magnetic field direction to the perpendicular. FID signals are measured maximum when net nuclear magnetization becomes perpendicular to the static magnetic field (the pulse angle = 90° to the static magnetic field, Fig.4B). After reaching maximum, if RF pulses continue, the net nuclear magnetization direction changes, and, the FID signal becomes zero when net magnetization aligns with the same course as the static magnetic field (the pulse angle = 180°, Fig.4C). If still, the RF pulse continues after 180° angle, the magnetization vector changes a direction, and signal amplitudes are taken negatively however maximum amplitudes don't change (Fig. 4 D). Acquisition of the FID signals is run by a receiver in the system and for interpreting, Fourier transform is used, and signals are transformed into frequency information.

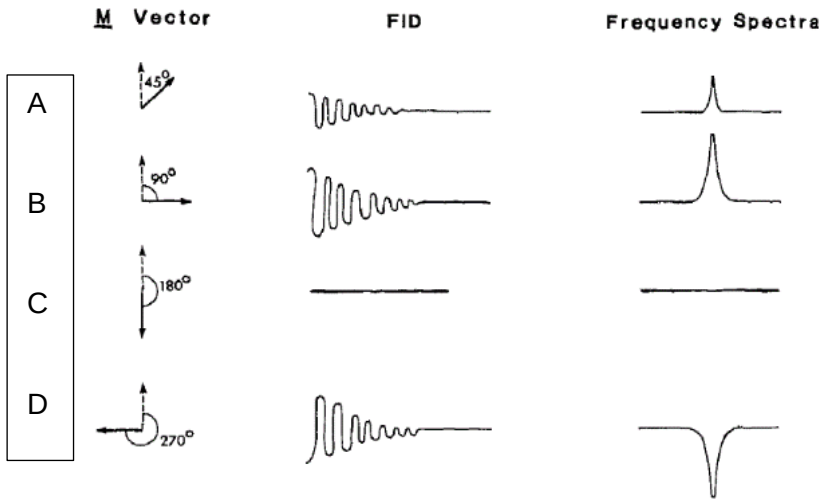

Figure 4: The schematization of FID by different pulse angles, and their frequency spectra after Fourier Transformation[36]. 4A shows FID decay which is obtained after 45° pulse angles and less than maximum FID. 4B shows a possible maximum signal obtained by 90°. 4C shows the pulse angle which does not produce FID signals and 4D shows a 270° pulse angle with the same magnitude as 90° but with a negative direction.

2.2.2 FID Interpretation: Relaxation Times

FID signals can be analyzed by two different methods with different receivers which are placed in different positions. T1 relaxation (longitudinal or spin-lattice) and T2 relaxation (transverse or spin-spin) are two different FID signals detected by receivers. T1 is calculated by using FID signals which are formulated as the "z" direction in the Bloch equation in the previous part, and T2 is calculated by using FID signals obtained from the "xy" plane (Equation 3).

As mentioned before, net nuclear magnetization reaches a maximum by RF pulses after a while, and it becomes perpendicular to the static magnetic field. When RF pulses are stopped, the nucleus begins to release energy absorbed. During this process, net nuclear magnetization returns to the first position by losing its energy (induction decay). T1 relaxation is measured in the same direction as the static magnetic field and T2 relaxation is measured at the transverse plane to the static magnetic field. At the maximum point of the net nuclear magnetization, since magnetization is perpendicular to the static magnetic field, T1 measured zero, and it increases in time until it returns to the first position and reaches the maximum. The time from the beginning (T1 relaxation = 0, net nuclear magnetization 90° to

the static magnetic field) to reaching % 63 of the maximum relaxation is known as T1 relaxation time[35]. More simply, T1 represents nuclei spins returning process to their equilibrium which is parallel to the static magnetic field. However, various T1 relaxations could be measured from distinct tissues even though atomic nuclei are the same because of "chemical shift" which means different compounds of macromolecule leads to different magnetization features on the same nuclei. Additionally, spin-spin interactions, magnetic field inhomogeneities, and magnetic susceptibility are the main factors that could affect the T1- T2 relaxations of atoms.

When the net nuclear magnetization is maximum, nuclei make precession together transverse to the static magnetic field (in-phase). However, because of the effects which are mentioned before, while some atoms of tissue in phase, some of the atoms could begin to decay. This situation is known as dephasing [33]. T2 relaxation begins when the net pulse angle is 90° and if dephasing occurs only due to spin-spin interactions, it is known as T2 decay (T2 relaxation). However, while other factors also affect decay, this is known as T2* relaxation (T2 star decay) [35,40]. When the transverse magnetization is maximum, it shows all nuclei are in-phase (maximum T2) and after the beginning of the decay, the T2 signal is decreased until

all nuclei become de-phased. The T2 relaxation time is calculated as the time from the beginning until the signal becomes 37% of the initial (maximum) value[41]. T1 relaxation and T2 relaxation are main signals which are used for the acquisition of magnetic resonance images.

2.3 Nuclear Magnetic Resonance Imaging

Magnetic resonance imaging of the body parts by using NMR requires the locating signals for creating an image matrix. In two-dimensional (2D) images, the "pixel" corresponds to subunits whose value is created by the nuclei NMR inside the sub volume, and the "voxel" represent 3D sub-units in 3D MRI. Phase encoding and frequency encoding are methods that are used for specifying sub-signal's locations and magnitudes and creating voxels/pixels.

Frequency encoding is the technique that is used detection of signals locations by applying static magnetic fields with different magnitudes to the different locations. As mentioned in the Larmor equation, the spinning frequency of the nucleus is affected by the magnetic field strength, and different frequencies could be created even with the same nuclei under different magnetic field strengths. Depending on that, a gradient magnetic field

provides separation of the sub-units by creating different spinning frequencies at different sub-volumes.

The phase-encoding is generated by making nuclei in-phase situations at different times. Even if FID signals have the same frequency and the same magnitude when the beginning relaxation times of nuclei are different, signals are obtained in different phases, and it is used for creating phase shifts between voxels of a line or row and provides locations of voxels. Phase encoding is made by turning on and off the gradient for short times [33,34,42].

Consequently, for obtaining 3D data, slices could be created by two different methods. One of these methods is using only phase-encoding. In addition to the row-line creation, creating slices by phase-encoding can provide thin slices but, an acquisition could take a long time[42]. On the other hand, each slice could be processed separately by frequency encoding, and it is called 2D multiple slice acquisition. However, in this process, RF pulses are sent to each slice separately, and because of that, neighbor nuclei are affected by magnetization. Consequently, the gap should be left between different slices to avoid receiving signals from nuclei influenced by multiple RF pulses, and this situation limits

reducing slice thickness. Finally, acquired signals are converted by the computers into k space and transformed into image data.

2.4 Flow MRI Principles

In the following years after MRI application began used in clinical sciences, scientists researched on visualization of flow characteristics in blood vessels by MRI. Phase mapping and time-of-flight techniques were some of the methods they experimented with. Since the time-of-flight technique could be affected by other sources besides the velocity of the nuclei, the experiments did not give the desired results. However, phase mapping was found affected only by phase-shifting produced by the flow and directly related to the flow velocity[34]. In 1986, Nayler et al. announced phase-contrast NMRI principles for recording and visualization of blood velocity. In this part, PC-MRI acquisition principles and limitations will be explained.

2.4.1 NMR of a Mobile Nucleus

For the magnetic field in the Larmor equation, it was emphasized the magnetic field represents specifically the strength that is affecting the subject nucleus not only a random position in the system. Accordingly, in the presence of a gradient magnetic field (a magnetic

field that is changing linearly with position) mobile nucleus will be affected by different magnetic fields during its movement. In this case, the magnetic field in the Larmor equation needs appropriate adjusting to calculate the exact magnetic field which is applied to the nucleus. The Larmor equation for the mobile nucleus could be expressed by:

$$B = B_0 + G_x x + B_i \tag{4}$$

which appends the magnetic fields (G_x: gradient in the x direction) which are, nuclei are exposed along the movement on the x-axis to the initial magnetic field (B_0) and local magnetic fields (B_i). In this frame,

$$\phi_s(T) = \int_0^T \omega(t)dt \tag{5}$$

could be used for the calculation phase signal (ϕ_s) which is created by the motion of the nuclei. With the usage of angular frequency ($\omega = \gamma G_x x$) the equation could be expanded as:

$$\phi_s(T) = \int_0^T \gamma G(t)x(t)dt\ . \tag{6}$$

For the solution of Equation 6, the position of the nuclei could be calculated by a series of time derivatives:

$$x(t) = x(0) + x'(0)t + {x''(0)t^2}/{2!} + \ldots + {x^n(0)t^n}/{n!} + \cdots \quad (7)$$

and finally, the formulation which could be used at directly calculation of velocity could be obtained:

$$\phi_s(T) = x_0 \left\{\gamma \int_0^T G_x(t)dt\right\} + \upsilon \left\{\gamma \int_0^T G_x(t)tdt\right\} + \alpha \left\{\gamma \int_0^T G_x(t)t^2dt\right\} + \ldots. \quad (8)$$

In this equation, inside of the integration of the first term represents the area under the gradient waveforms and it is recorded proportionally to the position (x_0) thereupon this term is known as position encoding. The second term is known as velocity-encoding and is found proportional to the velocity (υ). Generally, the third term which is proportional to the acceleration (α), and higher terms are accepted as negligible[20]. TE (the time between RF pulses and receiving to signal by the receiver) is used as duration and

$$\phi_s(TE) = x_0 \left\{\gamma \int_0^{TE} G_x(t)dt\right\} + \upsilon \left\{\gamma \int_0^{TE} G_x(t)tdt\right\} \quad (9)$$

gives the general formulation of phase signal[25,34]. Consequently, we could reach to phase equation

$$\phi = \nu\,(\gamma\, M_1) \tag{10}$$

which is created by the velocity of the nuclei by combining the first-moment equation ($M_1 = \int_0^{TE} G(t)t\,dt$) with the second term of Equation 9. However, since reasons mentioned before like magnetic inhomogeneities (B_i), pulse sequence timing errors, etc., the signal cannot be obtained purely and as a result,

$$\phi = \nu\,(\gamma\, M_1) + \phi_i \tag{11}$$

gives a more accurate approach to the velocity-dependent signal. In the equation, "ϕ_i" represents signals which are not created by the motion of the particle. Consequently, these errors lead to difficulty in observing correct flow velocity by single-phase measurement methods.

2.4.2 Phase-Contrast MRI Principles

The main idea of phase-contrast imaging is based on the clear-off of all effects than velocity and acquiring only flow-dependent signals from nuclei. For this purpose, another

magnetic field at the same magnitude but in the opposite direction is applied to the subject following the first magnetic gradient application (Gradient echo, Fig.5)[19,25,43]. In this way, even though all noise could not remove completely, unwanted signals created by the macro environment effect could be eliminated.

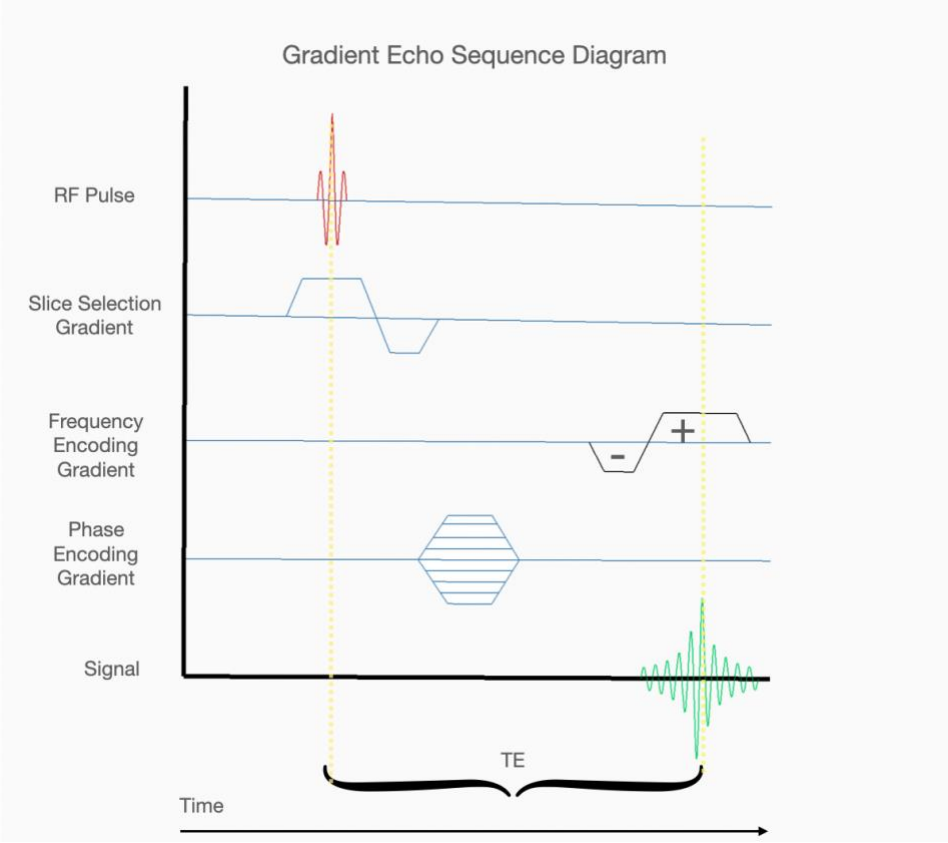

Figure 5: Gradient Echo diagram schematization with the application of opposite gradient fields. TE: Echo time

For the stationary particles which are protecting their first positions during scanning, magnetic gradient fields could be shown as:

$$G_s = G1 + G2 + Gi \tag{12}$$

same with Figure 6. Since the net magnetic field change will be zero ($G1$ and $G2$ magnitudes are gradient magnetic fields that have the same magnitude and opposite direction: Fig.6) and the result of the signal acquisition will be expected zero. However, due to unwanted effects, signals could be acquired from these particles which originated by Gi, and these signals correspond to the phase offset errors.

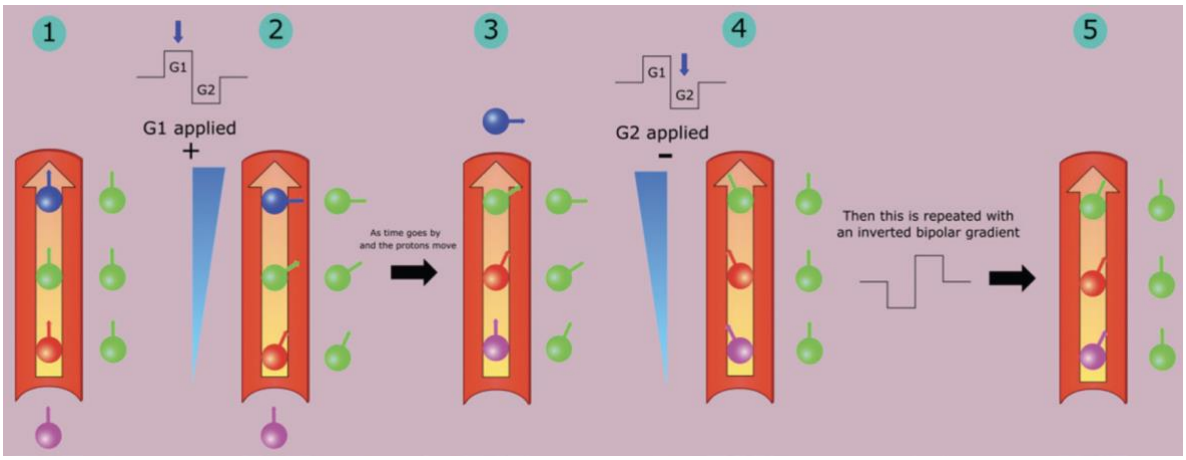

Figure 6: The schematization of the mobile nucleus and static tissue nucleus under applied bipolar magnetic gradient fields[44]. 1: initial, 2: after first gradian application, 3: after a while, 4: after second gradian application, 5: phase shifts due to atom's velocity.

In the contrast to the stationary particles, the magnetic field on the mobile nuclei change (red nuclei position in Figure 6.1 and Figure 6.3) following their motion, and the applied net magnetic field becomes different from zero on these nuclei[44]. The difference between phase signals obtained after bipolar gradients shows phase shift and could be formulated as:

$$\Delta\phi = \phi_0 - \phi_1 . \tag{13}$$

Since the bipolar gradients have the same magnitude and opposite direction (Figure 6; G1 and G2), the area under them is equal to zero and position term in Equation 9 is become zero, and the phase shift is found proportional to the velocity:

$$\Delta\phi = \nu\,(\gamma\Delta\, M_1) . \tag{14}$$

2.4.3 Velocity Encoding

During the explanation of FID signals, net nuclear precession changing under continuing RF pulses was explained. Depending on the gyromagnetic ratio, the maximum FID signal magnitude could be affected by the magnetic field but not RF pulses. It is necessary to remember FID signals are reaching a maximum at 90° pulse sequence and even in continuation of application, maximum FID is not changed but the direction changes and FID begins to decrease. When it reaches 180° it becomes zero and in the continuity of RF

pulses, it gives the negative signal until back to the first position. Consequently, maximum FID signal amplitudes of the nuclei could be changed only with the alteration of the magnetic field.

Since the detectable maximum FID signals by the nucleus are limited by the magnetic fields, also velocity could be measured in a specific range depending on this limitation. The maximum velocity that could be measured by the system is known as velocity encoding[20,25,43] and could be shown as:

$$\nu_{enc} = \pi/(\gamma \Delta M_1) \tag{15}$$

and when we connect the formula with Equation 14, we obtain the equation of velocity:

$$\nu = \left(\frac{\nu_{enc}}{\pi}\right) \Delta\phi \tag{16}$$

Depending on this limitation, for making the system capable of measuring velocity correctly, gradients should be adjusted appropriately because the system will never give the velocity magnitude higher than velocity encoding.

2.4.4 Four-Dimensional Flow MRI

Even though the velocity of the nuclei by NMR could be measured successfully, flow MRI imaging has a lot of difficulties depending on the complexity of the subjects which is measured. Localization of the signal, storage, processing data, and measured big areas are some of these difficulties. The solving of some of the difficulties in the flow MRI acquisition in time by the development in computer sciences like more powerful graphical units and advanced imaging techniques like kt-BLAST, kt-SENSE, and kt-GRAPPA enabled the short acquisition times[45].

Velocity magnitudes of the three different directions of the coordinate system could be obtained by changing the direction of the gradients, which is possible with additional gradient lobes, and 3D flow MRI could be obtained[19,46]. Additionally, multiple scanning could be done during the cardiac cycle, and a 4D flow MRI could be created. This technique allows for recording and visualization of body fluid velocities during a cardiac cycle. Usage of 4D flow MRI enables the detection of physiological and pathological flows and it could be used in the management of diseases.

2.5 Four-Dimensional PC-MRI Limitations

Four-Dimensional (4D) PC-MRI has a wide usage area in clinical and biomedical engineering science. In the introduction, the importance and indispensability of the PC-MRI were explained. However, depending on limitations generally raw data needs correction processes. Phase offset errors, weak temporal-spatial resolution, aliasing artifacts, wrapping artifacts, difficulties in choosing the region of interest (segmentation), motion artifacts, machine-related artifacts, etc. limit the usage of this technique[23,24,47–49] and lead to deviated results from correct data.

Development of the image acquisition techniques is helpful to increase temporal-spatial resolutions. However, partial volume artifacts could be seen at the border voxels which is including of fluids and tissues' nuclei together. Spatial resolution and manual segmentation of the region of interest (ROI) for quantitative calculations also could lead to inter/intra observer difference and subjectivity. Medical software programs (MIPAV, Medseg, etc.) supply segmentation and facilitate a more objective selection of ROI. Motion artifacts originated from patients' movements, and they may require re-acquisition. Wrapping artifacts are related to the field of view (FOV) and increasing FOV could fix these artifacts[48]. Aliasing

artifacts and phase-offset artifacts are caused by the PC-MRI acquisition principles, and they could be decreased during image processing by various interventions.

In this part phase offset artifacts, aliasing artifacts, and partial volume artifacts will be explained in detail and in the following chapters suggested correction methods will be explained for these artifacts.

2.5.1 Aliasing Artifacts

Aliasing artifacts occur when the velocity exceeds velocity encoding. When the signal is received by the receiver, it presents the magnitude and direction of the velocity. The expected velocity should be between $-\nu_{enc}$(-180°) and $+\nu_{enc}$(180°). Since the maximum velocity magnitude is restrained by velocity encoding, the velocity higher than that cannot be measured accurately. For example, when the actual velocity is equal to 1.1 * ν_{enc} , it makes (180° * 1.1) 198° . However, it is measured as -162° (- 0.9 ν_{enc})[20,25]. Consequently, if the true velocity is 60 cm/sec while ν_{enc} is 50 cm/ sec; the velocity will be measured as -40 cm/sec as deviated as a two-time fold of velocity encoding.

2.5.2 Partial Volume Artifacts

Partial volume artifacts are non-negligible errors, especially while the calculation area has a small diameter like small vessels and aqueducts cerebri. Depending on low spatial resolution, some voxels could represent both tissue and fluid information and it is shown that it generally leads to measuring flow rate more than the real value[50].

2.5.3 Phase-offset Artifacts

Phase offset errors represent deviations from the phase of nuclei because of unexpected effects and it leads to measuring different signals by the receiver. Three main sources are known as reasons for these artifacts: Eddy Currents, concomitant gradients, and gradient field distortions.

Gradient Field Distortions: The nonlinearity in the gradient field leads to geometrical distortions in the image. When the pixel/voxel sizes are different from each other means phase-encoding is used differently and it could lead to also geometrical distortions[49].

Concomitant Gradients: In flow imaging, the application of magnetic gradient fields additionally leads to concomitant gradients because of changes in the magnetic field strength and direction, and it leads to phase offsets. Concomitant gradient errors could be explained

by Maxwell's equation, and they are also known as Maxwell's artifacts[24]. Maxwell's errors are known proportional to the rate which is the square of the gradient to the static magnetic field (G^2/B), and are increased with a stronger gradient and/or weak static magnetic field[51]. Previous studies show that these concomitant gradient terms show quadratic spatial dependence[51].

Eddy-Current-based Phase Offset Errors: Even though the application of bipolar gradients simplifies the measurement of flow velocity by PC-MRI, the change in magnetic field direction triggers Eddy-current-based phase offset sources while decreasing errors of the beginning. The changing of the gradient fields' directions in PC-MRI, naturally leads to Eddy-currents and these currents affect the magnetic field of the nuclei unwantedly[23,24]. Eddy currents (Foucault currents) represent loops of electrical currents which are induced by changes in magnetic fields. These currents are built proportionally with the rate of change in the magnetic field according to Faraday's Law and create their own magnetic fields. PC-MRI is procured from phase shifts which are created by opposite gradient fields. Consequently, measured velocity is affected by these errors.

3. Objectified Phase Offset Error Correction in 4D PC-MRI

3.1 Introduction

Since phase offset errors are not negligible in PC-MRI, correction is an obligatory process for analyzing flow features correctly[24]. As mentioned above, phase offset errors are affected by many reasons including tissue features to acquisition principles, and depending on that, they may differ from person to person.

One of the correction methods for removing these errors is subtracting the mean velocity of a small area that is selected from brain tissue (stationary tissue) close to the ROI in recent CSF studies. In this method, the stationary tissue region may be chosen from around the aquaeductus (C shape) or from the close region of the pons[26,28]. While this technique is usable and easily applicable in clinical practice, unfortunately, the method is highly subjective because of the dependence on small, manually selected stationary regions, and the accuracy of correction cannot be interpreted.

In this chapter, the subject-specific automated correction method for phase offset errors will be explained. The method was built with the inspiration of previous research that is using the polynomial fitting, and it is integrated into CSF flow features[24,47]. The main difference

between this study and the inspired studies is the study area. While Lankhaar et al. suggested a phase offset correction method for main pulmonary artery flow[47], in this study, CSF flow was examined. Depending on that, some regulations were made specific to the CSF analysis and explained in the method section.

Features of the data used in the research were explained in the following section. For the understanding of the regression analysis compatibility, residual standard errors were shown. Additionally, background noise also was analyzed to evaluate data credibility.

3.2 Data Acquisition Principles and Features

In this study, 9 healthy persons and 9 iNPH patients' 4D PC-MRI data with 8-time phases were used. Data were obtained after oral and written informed consent by the Department of Neurosurgery, Shiga University of Medical Science Hospital in 2018–2020 were investigated. PC-MRI data were acquired from the cranial region at the sagittal plane at eight different points-time intervals equal through one normal sinus rhythm cardiac cycle by a 3-Tesla MRI scanner (Discovery MR750W, GE Medical Systems, Inc., Chicago, IL, USA) with a 24-channel head coil.

The data were continuously acquired, and selection was made retrospectively gated by interpolation as fractions of each R–R interval, which was synchronized with the peripheral pulse rate measured from the finger. Eight phases of the cardiac cycle were reconstructed, and cine frame times were between 91 and 123 ms. The self-calibrated data-driven parallel imaging reconstruction method "auto-calibrated reconstruction of cartesian" (ARC) data, 31 was used with an acceleration factor of 2. The spatiotemporal acceleration technique kat-ARC32 with an acceleration factor of 6 was used to reduce the scan time. The Maxwell term correction was applied in the vendor-provided reconstruction process. Three slices at either end of the 4D flow slab were removed before the error correction process, to avoid influence from the extra FOV. The total scan time was approximately 10 minutes.

The 4D-flow scanning parameters were as follows: repetition time (TR) = 20.6 ms/echo time (TE) = 2.00 ms; matrix 256 × 256; field of view (FOV) 200 mm, slice thickness 2 mm, slice interval 1 mm, and VENC 50 mm/s, flip angle 8°, and slab thickness 40 mm. The Maxwell term correction was applied in the vendor-provided reconstruction process.

3.3 Methods

3.3.1 Phase Offset Error Spatial Distribution Analysis

Before phase offset error analysis, infolding artifacts (wrapping artifacts) were cleaned by clipping data. After obtaining appropriate data, errors were estimated by using stationary tissue whose expected velocity is close to zero by polynomial regression analysis. After formulated phase offset errors, the corrected velocity map was created by extracting errors from raw data. Image processing was performed using the Insight Toolkit library (https://itk.org/), an open-source imaging library written in C++.

Velocity data which is obtained from each pixel of PC-MRI could be formulated as

$$u_i(x_1, x_2, x_3; t) = \hat{u}_i(x_1, x_2, x_3; t) + u_i^{off}(x_1, x_2, x_3; t) + \varepsilon_i(x_1, x_2, x_3; t) \qquad (17)$$

in general. In the equation, x_1, x_2 and x_3 represent coordinates of voxel in 3D and "i" values show velocity direction ((i = 1) u_1: left-right, (i = 2) u_2: anterior-posterior, (i= 3) u_3: inferior-superior) and t shows each different time phases. $u_i(x_1, x_2, x_3; t)$ is the raw velocity data that is read directly from PC-MRI, and $\hat{u}_i(x_1, x_2, x_3; t)$ is the true velocity which is expected without error. $u_i^{off}(x_1, x_2, x_3; t)$ gives the phase-offset error and $\varepsilon_i(x_1, x_2, x_3; t)$ is the background noise which is remained errors after correction of the phase-offset errors.

Stationary region velocities are accepted as equal to phase offset errors since zero velocity is expected in that regions. Depending on that, stationary tissue velocities were used for the prediction of the phase-offset error distribution, and it could be shown as:

$$u_i^{off}(x_1, x_2, x_3; t) = \sim u_i(x_1, x_2, x_3; t)\,. \tag{18}$$

The stationary tissue region was clarified based on temporal standard deviations (SD_i) throughout 8-time phases with the following equation:

$$SD_i = \sqrt{\frac{\sum_{t=1}^{t=8}(x_t - \mu)^{\,2}}{8}} \tag{19}$$

$$\mu = \frac{\sum_{t=1}^{t=8} x_t}{8} \tag{19a}$$

which have been used in previous studies and have been widely accepted [47,52]. Standard deviation throughout all time phases was calculated for each voxel separately and if the standard deviation is less than the threshold value ($SD_i < \lambda_{th}$) the voxel was accepted as a stationary region component. The threshold value was set as 2 mm/s to extract the stationary region appropriately without fluid regions including vessel and air regions. However, this method has some limitations in the discrimination of regular but high-flow regions such as

the venous system. To avoid these possible un-stationary regions, robust regression analysis M-estimator was used while polynomial regression analysis due to assuming that the velocity of these structures is much higher than the stationary region voxels.

It is shown that second-order equations are adequate for estimating phase offset errors in previous research [47]. In the light of that, second-order polynomial regression analyses were made for the formalization of phase-offset errors spatial distribution. The polynomial equation of regression could be summarized as:

$$u_i^{off}(x_1, x_2, x_3) = \sum_{p,q,r=0}^{p+q+r=2} a_{pqr} x_1^p x_2^q x_3^r \quad . \tag{20}$$

In the equation, p, q and r symbolize power of $x_{1,2,3}$ components, and p, q, and r features have been chosen as:

$$p, q, r \geq 0 , \quad p + q + r \leq 2 \tag{20a}$$

and 10 coefficients have been obtained for each case in this way. Coefficients were calculated with robust regression analysis by using M-estimator via R studio with a MASS package instead of least-square fitting because of stationary tissue disadvantages mentioned above.

An example estimation map that is created by the polynomial regression function were shown in Fig.7 and Fig.8.

In previous studies, the prediction function was created using time-averaged velocity data which could be calculated by the following equation:

$$u_i^{off}(x_1, x_2, x_3) \approx \frac{1}{N}\sum_{t=1}^{N} u_i\,(x_1, x_2, x_3; t) \tag{21}$$

In this approach, the phase-offset error is accepted the same at each phase and only one regression function is calculated for each data and each different time phase. Finally, estimated errors belong the per voxel were extracted from raw data and raw data were cleaned from phase-offset errors (Fig. 7.2).

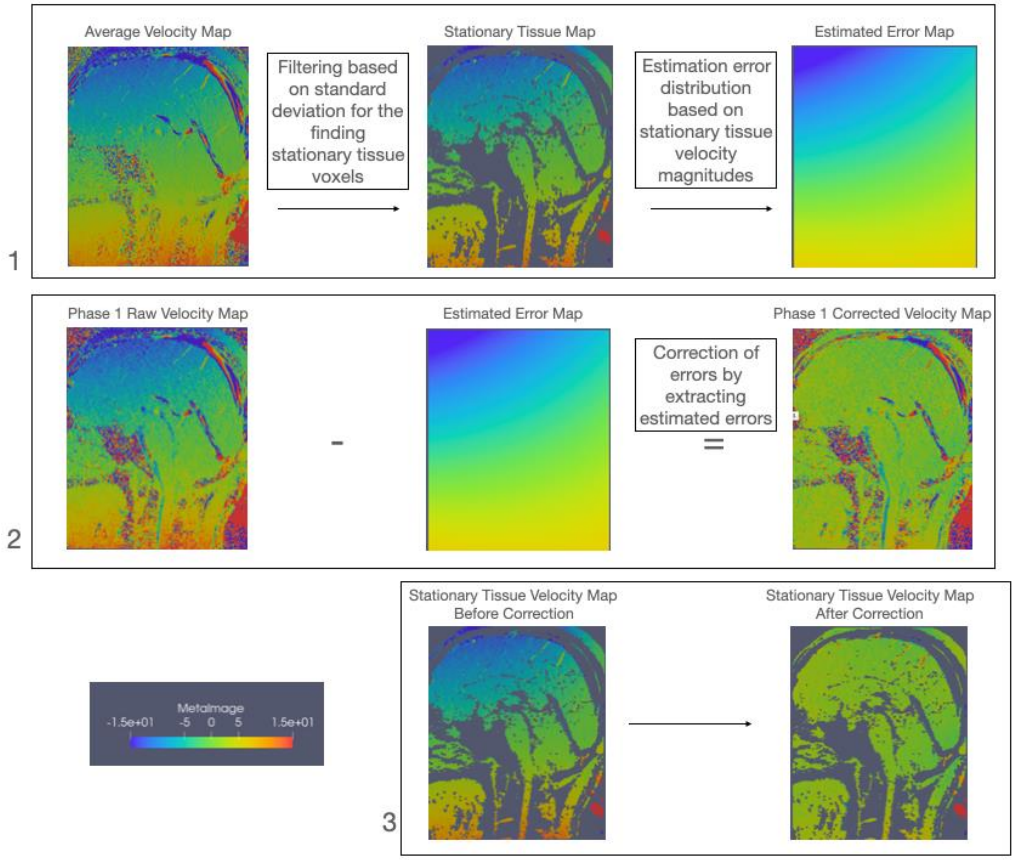

Figure 7: Representation of the velocity maps before and after correction with estimated stationary tissue and phase offset error map.

7.1 shows the estimation of error distribution from the stationary tissue velocity map which is obtained by a standard deviation filter.

7.2 shows the correction of the Phase1 velocity map of the representative case by extracting estimated errors.

7.3 shows only the corrected stationary tissue average velocity map.

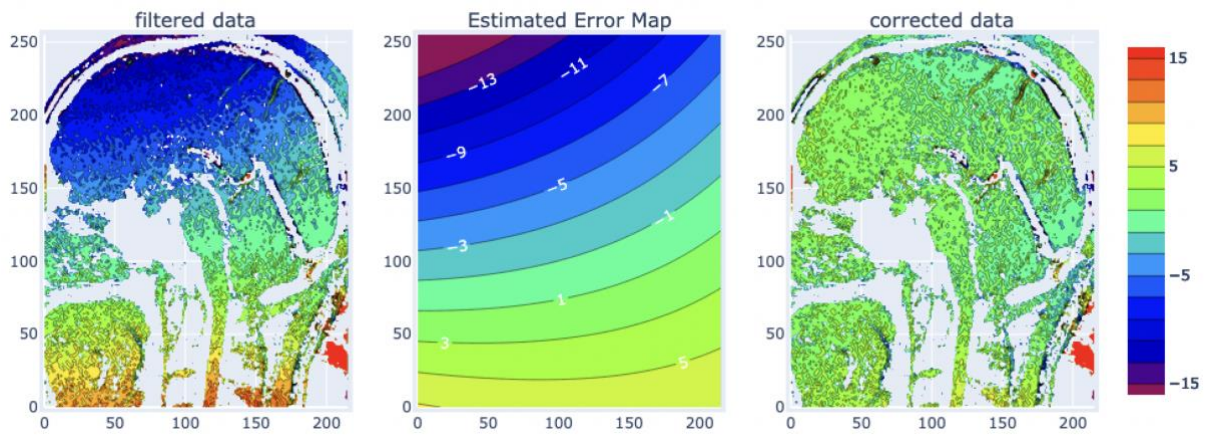

Figure 8: The representative case stationary tissue velocity distribution before (filtered data) and after correction (corrected data) with the estimated error contour map.

3.3.2 Evaluation of Regression Analysis and Background Noise

Consistency between prediction function and stationary tissue was evaluated by residual standard errors. Spatially distribution of phase-offset errors was examined with coefficients magnitudes which are linked to coordinates of voxels. The distribution of phase offset errors and background noise that remains after the correction was shown for the visualization of the method efficacy. Spatial standard deviations and averages of background noise were given to show the usability of the corrected data.

3.4 Results

The residual standard errors represent consistency between raw data's stationary tissue velocities and the estimated phase-offset errors obtained by regression analysis were found under 1.7 mm/s for each case and each velocity direction. Figure 9 shows 18 cases' residual standard errors separately for each velocity direction. For the superior-inferior and left-right direction velocities, maximum errors were found under 1.25 mm/s.

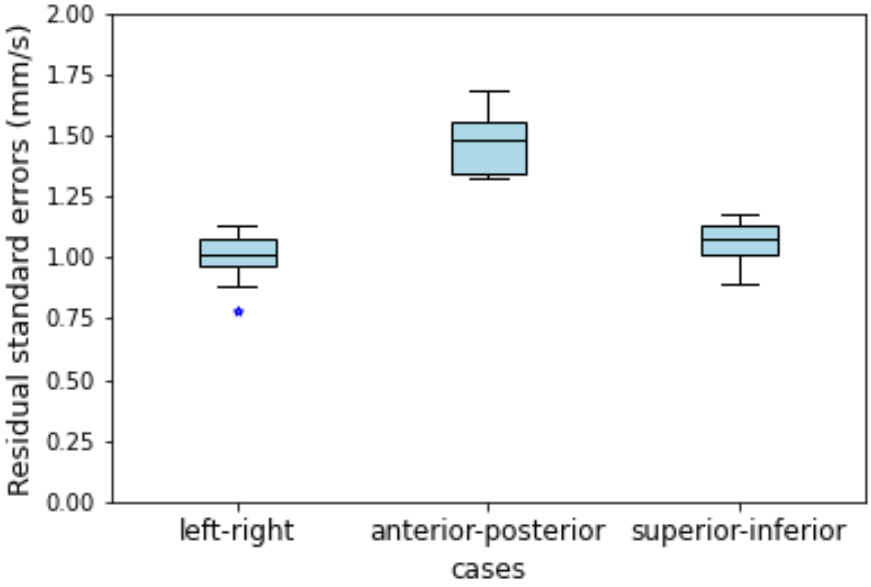

Figure 9: Residual standard errors distribution throughout all cases at each velocity direction.

Figure 10 shows the coefficients box plot which is acquired from per case polynomial regression equations. The columns in the figure show same-order coefficients, but each cell belongs to different velocity directions. Constant values ranged between -2 and 10 mm/s for each case, first-order coefficients between -0.1 and 0.14, and second-order coefficients ranged between -0.12 and 0.01. However, a similar tendency to spatial dependence was not seen between different cases and different velocity directions as could be seen in Figure 10.

The error values were examined also by calculation of mean and standard deviation values of stationary tissue velocities for raw data (before correction) and corrected data. While the mean of errors was obtained from -8 to 10 mm/s in the raw data, the values were decreased to between -1 and 3 mm/s by correction of phase offset errors. Standard deviations were decreased in each velocity direction after correction as could be seen in Figure 11's first row.

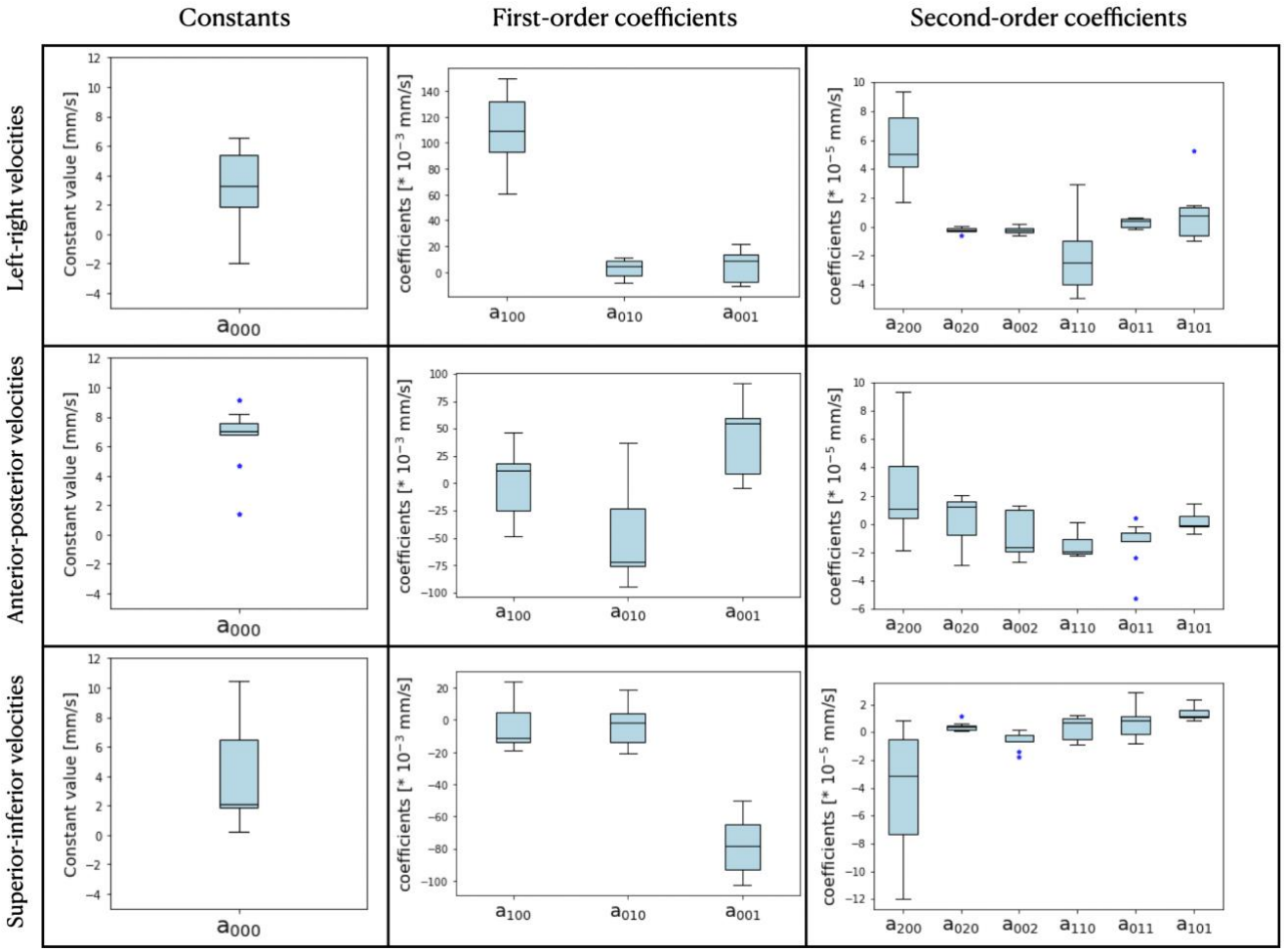

Figure 10: The figure shows all cases' coefficients of the polynomial equation calculated by regression analysis. Each column shows different order coefficient box plots, and each row belongs to a different velocity direction.

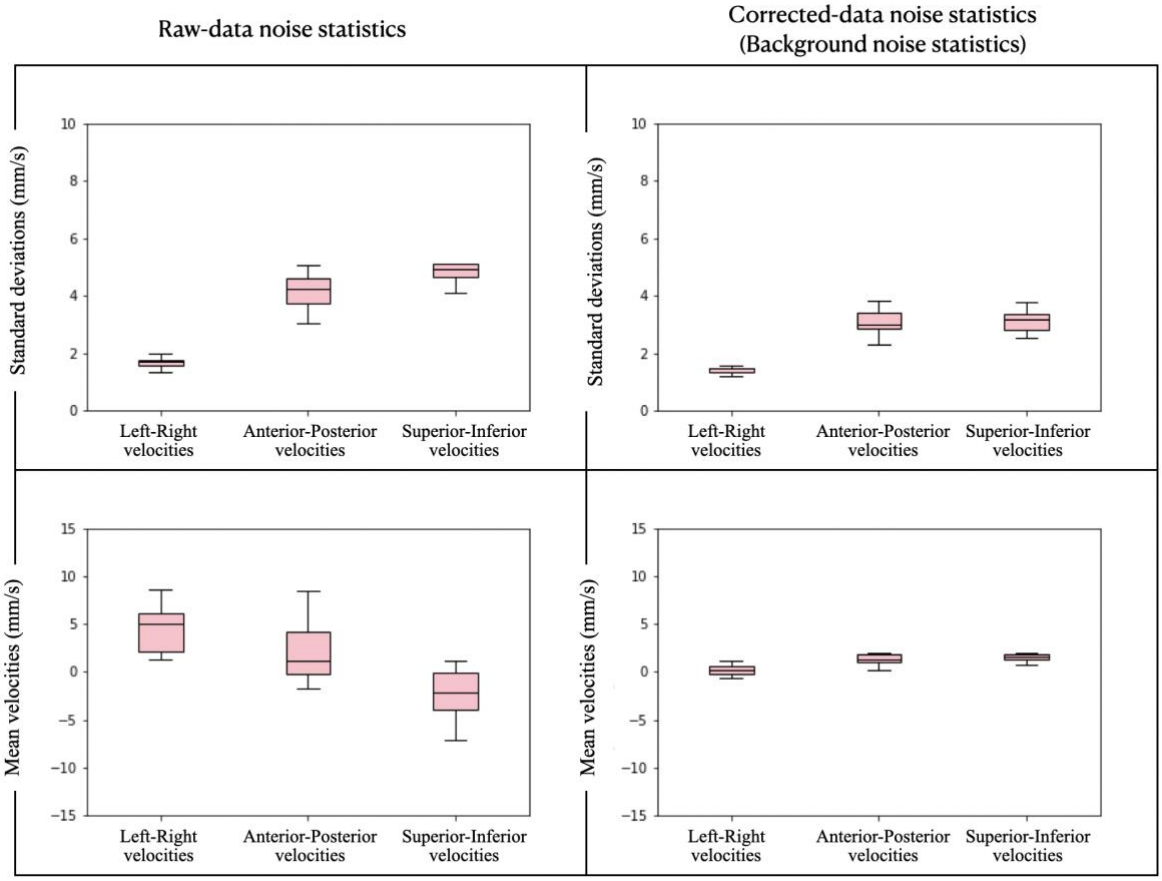

Figure 11: The figure shows the standard deviation and the mean values of stationary tissue velocities of 18 different cases before and after correction. The first column shows statistics from raw data and the second column shows statistics belonging to corrected data.

For the visualization of the phase offset error effect on all voxels, all stationary voxels' velocities belonging to each case and direction were given as a box plot in Figure 12. Uncorrected and corrected data values were shown in different columns for comparison. The first column presents the velocity distribution of each case and each direction obtained from raw data. The second column shows the stationary tissue velocity distribution after correction of phase offset errors, and these remained errors are known as background noise.

Figure 12 shows the range of error values decreased from -5 and 10 mm/s to -3 and 3 mm/s for the left-right direction. For the anterior-posterior direction, the range decreased from -18 and 20 mm/s to -5 and 5 mm/s except for case 13. In the superior-inferior directions also range decreased from -25 and 20 mm/s to -5 and 10 mm/s except in case 13. Unfortunately, case 13 errors could not be decreased as much as in other cases in the superior-inferior and anterior-posterior direction and some voxels background errors remained more than 10 mm/s.

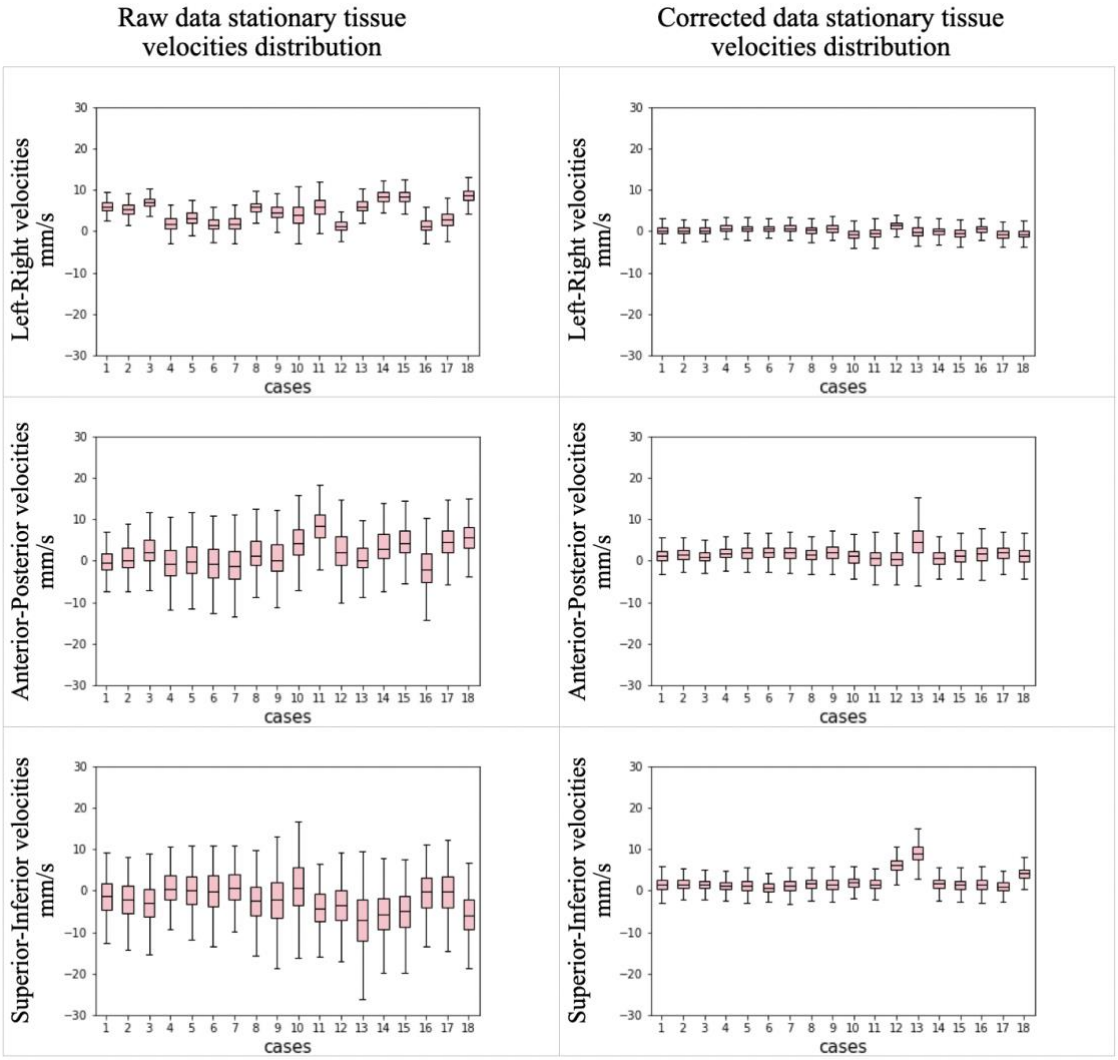

Figure 12: The figure shows all stationary voxels' velocities distribution before and after correction in each velocity direction. Each row shows different velocity direction values and while the first column shows raw data values, the second column shows corrected stationary tissue velocities' distributions. Each graph in cells includes all case's stationary tissue velocities distributions.

3.5 Discussion

Phase offset errors are known for a long time and previous CSF research with PC-MRI handled these errors by using local correction approaches[27,28]. The local approaches include choosing a reference area close to the ROI to estimate phase offset error and this process is made by calculating the spatial average velocity of reference area pixels[26]. The spatial average value is accepted as phase offset error, and it is subtracted from each pixel in the CSF flow calculation area. Depending on that, the local correction methods don't provide an evaluation of the background noise, data quality, and correctness of the calculated phase offset error. Besides, local correction methods limit the study area to 2D and require manual interventions. In contrast to local correction, the automated 3D correction method was suggested in this chapter. This method provides objectivity in the correction with not requiring manual intervention. Additionally, the presented method enables evaluation of the data quality which provides residual standard errors and background noise (Figure 9, Figure 12). In this way, the data which does not have qualified for the analysis even after correction could be removed from the studies. Most importantly, the correction method creates a 3D

environment for analyzing CSF flow and it does not limit the research area, unlike local correction methods.

On the other hand, this study has limitations because of the number of cases and working with the data acquired by the same principles. For example, since Case13 background noise was found clearly more than in other cases it was excluded from further calculations. However, the case number was inadequate for building any parameter, depending on that, exclusion or inclusion parameters for data could not be built.

4. Objectified Approach to Calculation of Flow Rate in Aqueducts Cerebri

4.1 Introduction

PC-MRI gives quantitative information for the discrimination of iNPH and other diseases and helps to diagnose [43,53]. Generally, calculations are done on the 2D slice, which is taken from around mid-aqueductus cerebri, and flow features are measured like flow rates, peak velocities, stroke volume, etc[29,31,32]. For example, Ahmad et al. showed that peak systolic velocity, peak diastolic velocity, and stroke volume were increased in iNPH patients compared to healthy cases, and on the contrary, in patients with brain atrophy these parameters were found to decrease[54]. While the calculation of stroke volume has many approaches by different studies[55,56] flow rates (q(t)) generally is calculated by summing velocity (*V*) and area (*A*) multiplication of each pixel in the region of interest (ROI) [28,55]:

$$q(t) = \sum_{r \in ROI} V_r(t) * A_{Voxel} \tag{22}$$

The maximum flow rate at the superior-inferior direction is known as the peak systolic flow rate, and the maximum flow rate at the inferior-superior direction is known as the peak diastolic flow rate and maximum velocities at these directions are known as peak systolic velocity, and peak diastolic velocity[57]. However, PC-MRI parameters for the

evaluation of CSF are still under debate and are not accepted as a diagnosis criterion while PC-MRI is the main diagnostic tool in cardiovascular research, and PC-MRI limitations could be shown as the main reasons. Limitations of PC-MRI were explained in Chapter 2, and the correction method for phase offset errors which is one of the biggest limitations of PC-MRI was suggested in Chapter 3. However, not only phase offset errors, but also aliasing artifacts, partial volume artifacts, and selection of the ROI could affect the results during the analysis of CSF flow. [43,58]. These artifacts generally are corrected manually, and it leads to subjectivity and waste of time.

In this chapter, automated correction approaches to aliasing and partial volume artifacts and semi-automated approach for ROI choosing were presented for improving objectivity and reaching repeatable and researcher-independent results. Before giving correction methods, these artifacts were explained in the following sections in detail. For the selection of the ROI, the semiautomated method was suggested by using MIPAV (Medical Image Processing, Analysis, and Visualization). After whole ventricles segmentation was made by MIPAV, aquaeductus cerebri was detected by an algorithm written in C++ automatically. For the correction of aliasing artifacts, inspired by the previous research which

used ultrasonography data[59]. For the partial volume correction, previous research approaches were integrated into automated data analysis[50]. After corrections, peak systolic and peak diastolic flow rates were calculated in aqueduct cerebri. In the results, flow rates and areas of aquaeductus cerebri were compared by the Man-Whitney U test between iNPH patients and healthy cases.

4.2 Effects of ROI Selection on Flow Measurements

For avoiding subjective and controversial results, ROI needs to be detected with minimum manual intervention or automatically if possible. For this purpose, automated segmentation could be applied if possible. K-means clustering, threshold methods, etc. with geometry data or velocity data were applied in plenty of cardiovascular research for automated segmentation of blood vessels [58,60,61]. However, big vessels' flow features and CSF flow features are hugely different. While blood velocity can vary around 20 cm/s in the internal carotid artery[62], and around 250 cm/s in the aorta [63], the cerebrospinal fluid velocity is expected in aqueducts cerebri to be about 5-8 cm/s[43]. The high flow velocity in blood vessels, smooth geometry, and clearly different magnitudes between vessels and neighbor tissue make vessels' segmentation more untroublesome.

Unfortunately, depending on the complicated geometry of ventricles and the slow flow of CSF makes mostly complicated ROI segmentation. Depending on that, CSF flow quantitative measurements by PC-MRI generally stay limited to a single slice of aqueduct cerebri in clinical sciences [31,53,64].

4.3 Aliasing Artifacts and Partial Volume Artifacts' Effects on Flow Measurements

When the voxel velocity is exceeded velocity encoding, the phase of nuclei is changed by more than 180 degrees, and it results in measuring the voxel's velocity differently from its real value. Aliasing artifacts' existence could be found by the calculation of differences between neighbor voxels/pixels of the flow MRI data. In the application, aliasing artifacts are accepted when neighboring velocities' difference' absolute value is detected more than velocity encoding (V_{enc}), and aliased voxels velocities (V_{raw}) are corrected in studies with the following equation[28,50]:

$$V_{corrected} = V_{raw} \pm 2 * V_{enc} \tag{23}$$

by adding 2-time fold V_{enc} to the detected aliased voxels in the appropriate direction for one-degree aliasing. However, finding differences gives aliasing pairs but does not indicate which one is the aliased voxel, and these corrections are being made manually by observers in CSF

research on 2D, and it is making the results observer-dependent. Besides, while aliasing artifacts tried to be corrected depending on a single slice, it could lead to wrong assumptions because when all voxels of the slice have an aliasing artifact, the artifact could not be realized.

Aliasing artifacts are not specific to the PC-MRI data and could be seen in ultrasonography measures, and some approaches to the automatic correction of these artifacts were suggested by researchers[59,65]. Unfortunately, the automated correction of aliasing artifacts in 3D CSF fluid flow was not mentioned in previous research. However, evaluation in 3D is necessary to find the aliased voxels for avoiding wrong results because of the possibility of wholly aliased 2D data (Figure 13). Depending on that, finding aliased voxels requires another process. This process was handled in previous studies about big blood vessels, by making segmentation and accepting a big segment as a correct and a small segment as an aliased segment which includes aliased voxels[59]. These studies applied the correction equation (Equation 23) to all voxels of the aliased segment and obtained corrected velocity maps. However, since, ventricles and big vessels' geometry and velocities are completely different, aliasing correction in CSF flow needs a specific approach. In the

method section, an automated approach was explained for the correction of aliasing artifacts in aqueduct cerebri with the inspiration of previous studies [59,65].

Partial volume artifacts originated from low spatial resolution. Because of the low spatial resolution, some voxels include fluid and stationary tissue' nuclei together. This situation leads to wrong calculations for flow rate depending on a lack of knowledge about flow area and real velocity information of fluid. Partial volume artifacts were known as a reason that could lead to a fraudulently increase in a flow rate [50]. In recent works, the importance of correcting these artifacts was shown and Bouillot et al. suggested a semi-automated method for the correction of these artifacts[50].

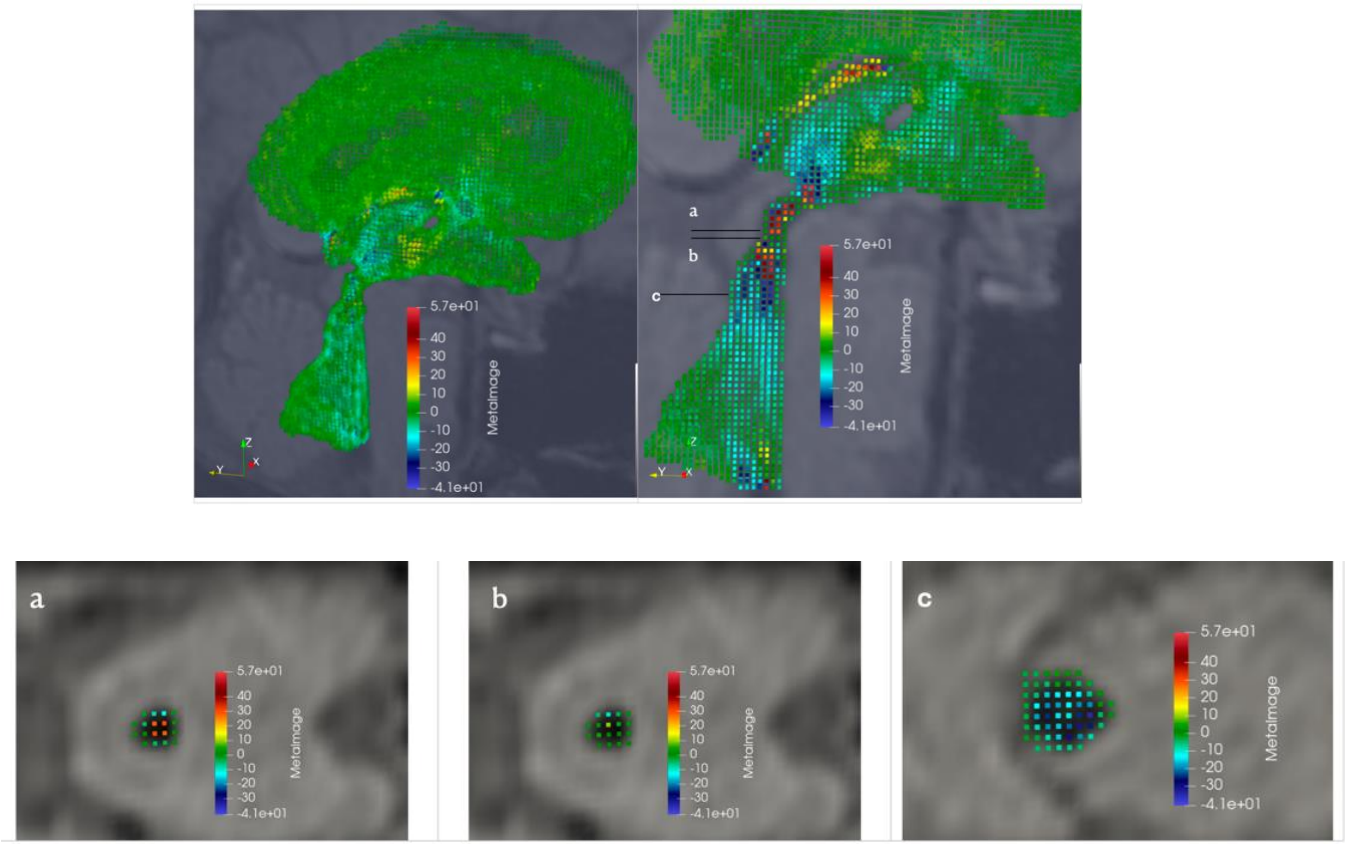

Figure 13: Representation of velocity maps that are obtained from different stages of aqueducts cerebri. The left image in the upper represents the 3D velocity map of the representative case. a, b, and c show velocity maps from different stages and the right image at the upper shows the sagittal plane of the 3D data and the chosen a, b, and c velocity maps' stages. 13a: axial CSF velocity map which does not show any aliasing artifacts, and the direction flow measured as from superior to inferior. 13b: the velocity map measured around zero velocity, does not have aliasing. 13c: The velocity map shows the flow from inferior to superior and does not have aliasing.

4.4 Methods

4.4.1 Semi-automated selection of VOI

For the analysis of CSF in aqueduct cerebri, ventricles were extracted in 3D from flow MRI data by using MIPAV (Medical Image Processing, Analysis, and Visualization; Center for Information Technology, USA) initially. The suggested segmentation process includes a bilateral filter and Fuzzy-C-means hard segmentation. While segmentation, firstly, the volume of interest (VOI) was created manually in 3D. Following ventricle segmentation, aqueduct cerebri was detected by using an algorithm written in C++ automatically.

The important point of the ventricle's segmentation process is that manually selected VOI was not used as a calculation area. VOI was chosen as a bigger area than the calculation area. During the process attended to include as much as stationary tissue around ventricles to the VOI (Figure 14). This process's aim is to obtain area for segmentation of ventricles rather than segment ventricles directly. After obtaining VOI in one time-phased, the same VOI was copied to all other time phases. To decrease the noise of images and increase resolution, the bilateral filter was applied to whole 3D images before choosing VOI borders. A bilateral filter was used to remove noises while protecting borders. After that, VOI is segmented into

two sub-volumes by Fuzzy-C-means hard segmentation. While this segmentation, classes were chosen as two for the VOI. This segmentation aims maximization similarity between the same group of voxels and minimizes similarity between different groups of voxels.

Consequently, stationary tissue and ventricles were separated automatically by MIPAV (Figure 15). In figure 15, the green area and red area together represent the selected VOI. The red area represents stationary tissue, and the green area represents the ventricular area which is obtained by the segmentation process. Figure 16 shows an example of ventricular segmentation's result in 3D.

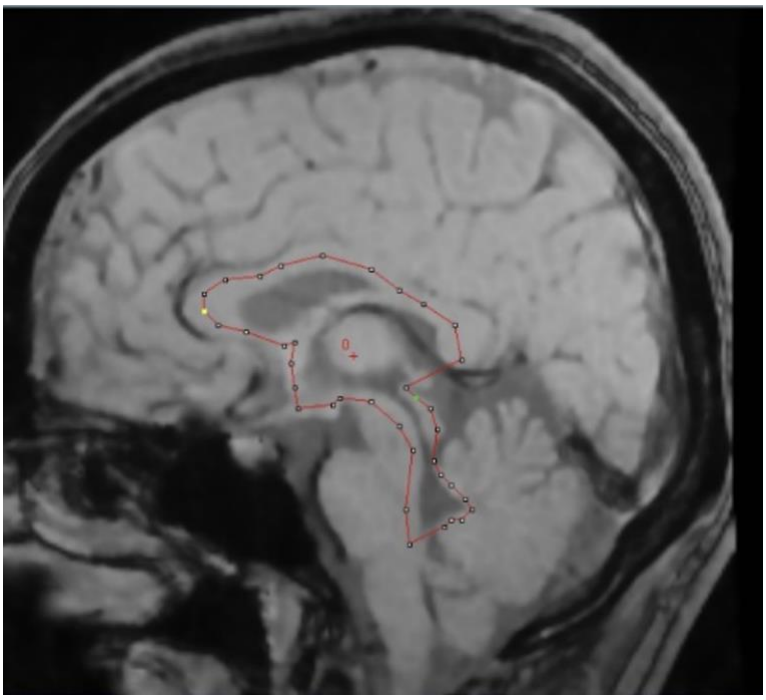

Figure 14: Selection of the VOI. The Red line shows VOI borders which were determined manually at one sagittal slice.

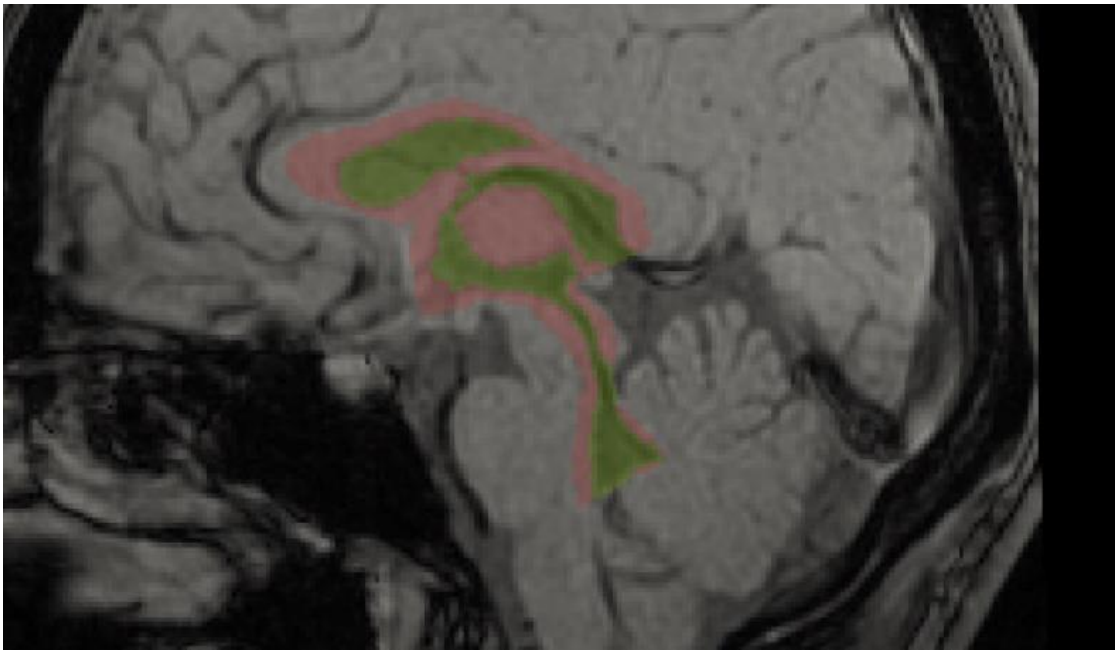

Figure 15: Representation of segmented ventricles at the sagittal plane by MIPAV. The Green area shows ventricles, and the red area shows tissue around ventricles.

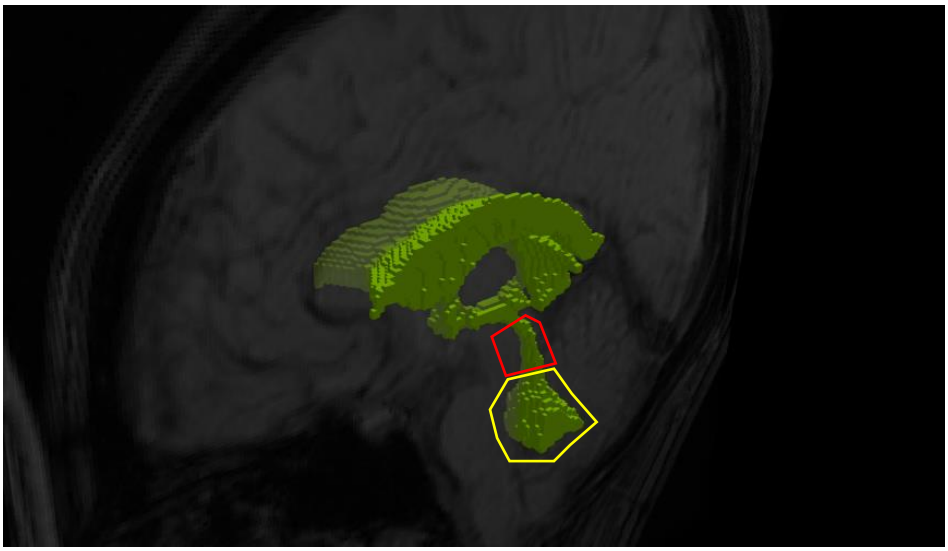

Figure 16: Representation of segmented ventricles in 3D. The region inside the red shape is the aqueduct cerebri, and the region inside the yellow shape is the fourth ventricle.

After ventricles segmentation, aquaeductus cerebri borders were chosen automatically by a program written in C++. For the finding aqueducts upper and bottom border, the algorithm below was followed:

1. The bottom point was found and accepted as an initial point.
2. With the following point, a map was created from the bottom to the upper. The important part of the step, while creating the map always continued from bottom to upper.
3. After the creation of the map, the stage which has the narrowest area was accepted as belonging to the aqueducts. In this step, the length was calculated and %10 from the beginning and top were not included to find the narrowest area for not choosing the bottom and upper slices as the narrowest area.
4. After finding the narrowest area, with the beginning from the narrowest area's stage, each stage was followed until the area was found to equal or more to the 2-time fold of the narrowest area. When the area was found, the stages until that there were accepted as an aquaeductus cerebri member. In this way, the upper border and bottom border of aqueduct cerebri were found (Figure 17b).

5. Calculations of CSF flow were made between the upper quarter and bottom quarter of the selected aqueducts region for avoiding border regions that are neighbors with the third ventricle and fourth ventricle (Figure 17c).

During the process, the second step of the algorithm was planned especially for iNPH patients. While healthy subjects' ventricles geometry as expected, some iNPH patients' third ventricles were extending nearly aqueducts cerebri, and without making a map from bottom to upper, finding directly the narrowest area could result in finding wrong stages because the third ventricle's parts could be accounted in aqueducts stages. The borders of aqueduct cerebri were used in the aliasing correction and calculation processes.

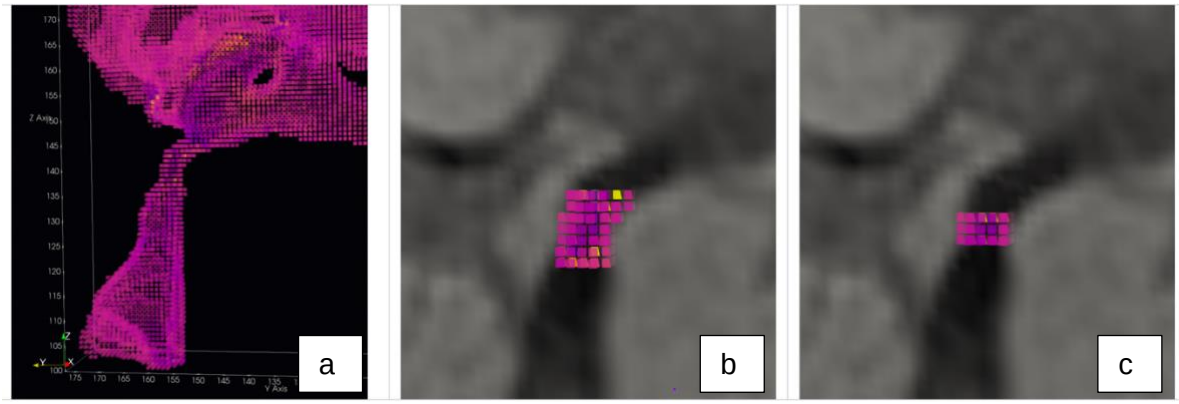

Figure 17: The figure shows the selected aqueducts cerebri region. 17a: whole ventricles visualization in 3D. 17b: VOI between the selected upper border of the aqueducts cerebri and bottom border of the aqueducts cerebri. 17c: Selected VOI for the running calculations for CSF flow in the aqueducts cerebri.

4.4.2 Anatomy-Based Automated Aliasing Correction

Aquaeductus cerebri is a region like a channel and depending on that it is also known as the aqueduct channel. This feature of aqueduct cerebri enables flow rate calculations in the axial plane in the superior-inferior direction. Aquaeductus cerebri continues with the fourth ventricle. The fourth ventricle has a wider area than aqueducts cerebri and consequently, the flow is slower in this region (Fig 16). Since aliasing artifacts are seen when the fluid velocity is higher than velocity encoding, it is more expected in aqueduct cerebri than in the fourth ventricle. With the inspiration of this idea, the fourth ventricle was followed for the finding of non-aliased voxels, flow direction in aqueducts cerebri, and aliased voxels. The algorithm was written in C++ language. During the process, the most important step was finding a flow direction through aqueducts cerebri and the fourth ventricle. Since other ventricles don't have channel-like shapes the fluid flow direction doesn't have to be the same at each voxel of them. Depending on that, lateral ventricles and third ventricles were not included in correction in this study. However, for the visualization, the area between the third ventricle and aqueduct cerebri was examined with the following only aqueductus cerebri voxels.

The correction process could be separated into two main steps. In the first step, CSF flow direction was detected if it is from superior to inferior or from inferior to superior. For finding the direction of the fluid, not-aliased voxels were marked on a map with the same sizes as the velocity data (Figure 18). This map was used during the process, and it will be mentioned as a 'reference map' in this study. The main direction of fluid was found by following steps:

1. The largest stage of the fourth ventricle was found as a less expected aliased region.
2. A reference map was begun from the largest stage of the fourth ventricle, and it was expanded to the upper and bottom, until finding the first aliased pairs. In this process, the voxels were marked as not-aliased voxels until aliased pairs appeared (Figure 18).
3. After finishing the creation of the reference map, the maximum velocity was found among marked voxels, and the maximum velocity direction was accepted as the CSF direction in aqueducts cerebri.

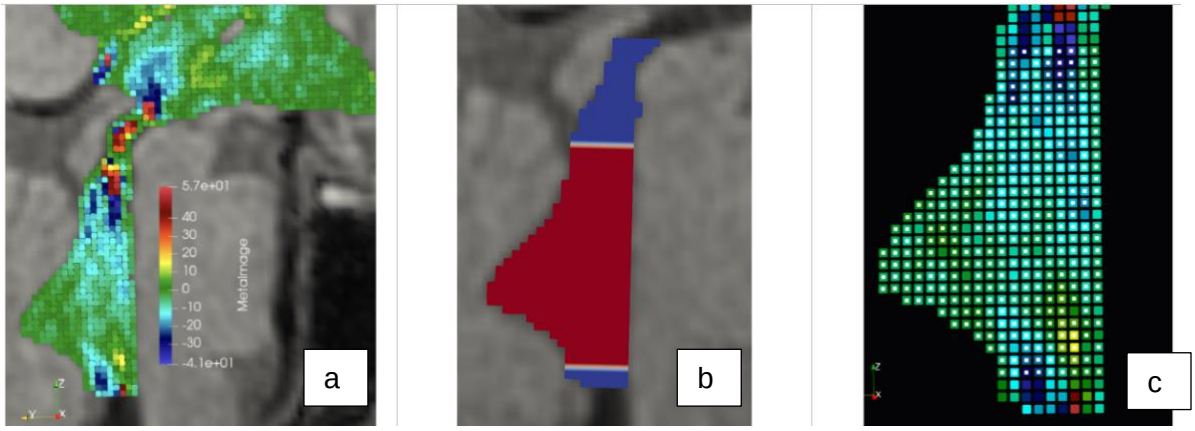

Figure 18: The visualization of finding the flow direction of CSF. 18 a: the velocity map of superior-inferior direction CSF flow in the representative sagittal plane. 18 b: The reference map was described in this section. The red area represents an accepted non-aliased voxels region. The blue area represents a suspected region that has non-aliased and aliased voxels together. 18 c: The velocity map with white marks shows non-aliased voxels based on the reference map for finding flow direction.

After finding the direction of the flow, voxels were corrected in the second part of the correction process. For avoiding over-correction and inadequate correction, the process was completed with 6 iterative functions. In the first step, segment corrections were made and in the other steps, voxels were evaluated along with their neighbors. In the segmentation process, making segments with the most similar voxels and separating different voxels' groups were aimed. This step was gained to system a possibility for correcting big, aliased groups at the same time and made the correction process less complex. The segmentation process includes the following steps:

1. Finding all neighbors' differences and recording their absolute values.
2. After finding all differences, the threshold value for separating neighbors was calculated by using the interquartile range (IQR). The threshold was accepted to be equal to the summing of the upper quartile and 1.5-time fold of IQR.
3. Based on the selected threshold value, neighbor pairs were separated into two groups. The pairs whose absolute difference was less than the threshold value was allowed to be in the same segment.

4. The pairs whose absolute difference was more than the threshold value were accepted as the stop criteria for the merging segments and voxels, and before merging segments and voxels they were controlled if there is any prohibited voxel for being in the same segment.
5. Merging was processed with the beginning from neighbors which have the smallest difference and continues with increasing until all voxels take a segment mark in order.

Choosing stopping criteria in this way for separating segments enabled to make appropriate segmentation of each different data. In contrast to choosing a specific value, this approach was followed for avoiding over-corrections. The segmentation results of a representative case could be seen in Figure 19. During this chapter, positive values in the velocity maps represented the fluid flow from super to inferior, and negative velocity values will represent flowing from inferior to superior.

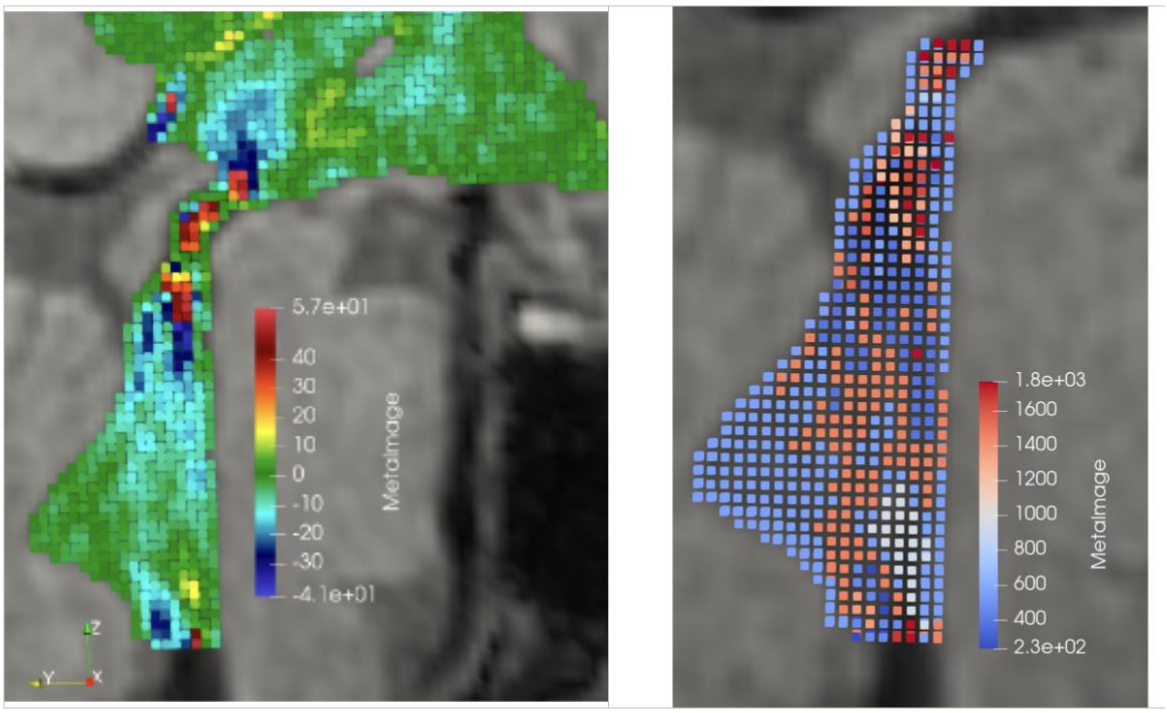

Figure 19: Visualization of the segmentation results of voxels. The left image represents the raw velocity map at the sagittal plane and the right image shows segmentation results of voxels in aqueducts cerebri and fourth ventricle.

After segmentation and finding the flow direction, correction steps were begun. The main aim of correction in the six steps was to make corrections under control and to avoid over or inadequate corrections. For this aim, the correction was begun with the segment's correction and in this step, aliased pairs were examined. Depending on the flow direction the aliased segments were detected and after checking the segments members' flow direction, aliased segments were corrected, and this process continued until there is no change in the velocity map. After the segment correction step, the correction of data was completed by 5 different iterative functions respectively (Table 1). The aim of the separating voxel correction phase into 5 steps was to make corrections under control by giving priority to voxels with a high possibility of aliasing. These steps were set based on determining the possibility of aliasing. In this aim, the voxels were selected based on exclusion criteria and, selected voxels were evaluated for the correction at control points. Control points represent the evaluation of aliasing possibility by calculating the difference with neighbor voxels like in previous studies [28,50]. However, for avoiding choosing the wrong voxels as aliased from aliased pairs, in the beginning, only aliased voxels that are found as a pair with referenced voxels (accepted as not-aliased voxels which are marked on the reference map) were corrected. In each iterative

function, evaluated voxels were increased step by step by changing exclusion criteria and control points (Table 1). After each function, the reference map was updated by marking voxels that are accepted not aliased depending on their relations with neighbors.

The velocity map changing after some iterative functions was given in Figure 20. Six correction steps were processed in aqueducts and the fourth ventricle. However, for the visualization, the area of the upper aqueduct cerebri was corrected. For this purpose, another three iterative correction functions were used. In these functions again same steps were followed. However, only segments that are a neighbor with aqueducts cerebri were corrected if their aliasing is in the opposite direction to the flow direction. In Figure 21 velocity maps before and after correction were given in their own appropriate velocity ranges with three different time phases of the representative case.

Table 1: The different features of iterative functions which are used during the correction of aliasing artifacts in the region below the upper aqueducts stage.

Iterative Functions	Inputs	Control Points	Features for exclusion
IterativeFunction1: Segment Correction	Aliased pairs	Segment direction	Mean velocity with different direction
Iterative Function2: Voxel Correction	Velocity map	Control aliasing with other neighbor marked in reference map	Border voxels Before corrected voxels Different flow direction
Iterative Function3: Voxel Correction	Velocity map	Control aliasing with other neighbor marked in reference map	Before corrected voxels Different flow direction
Iterative Function4: Voxel Correction	Velocity map	Control aliasing with all neighbors	Before corrected voxels Different flow direction
Iterative Function5: Voxel Correction	Velocity map	Control aliasing with not-border voxels	Before corrected voxels Different flow direction
Iterative Function6: Voxel Correction	Velocity map	Control aliasing with all neighbors	————

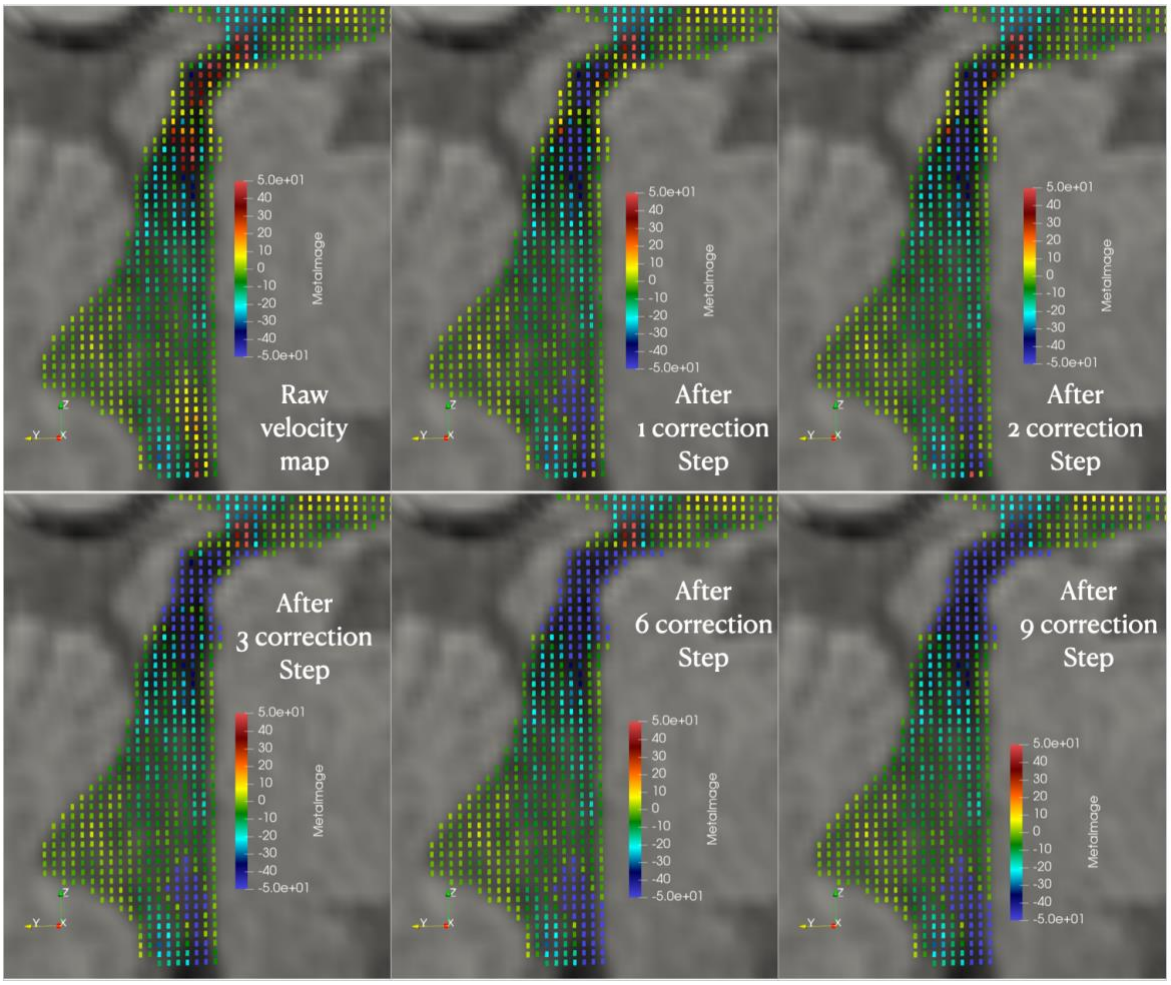

Figure 20: Velocity maps of the raw data, and after different correction steps. In the first 6 steps, only the region below the upper aqueducts cerebri stage was corrected and with the last three iterative functions, the voxels which have bound to the aqueducts cerebri were corrected for the visualization.

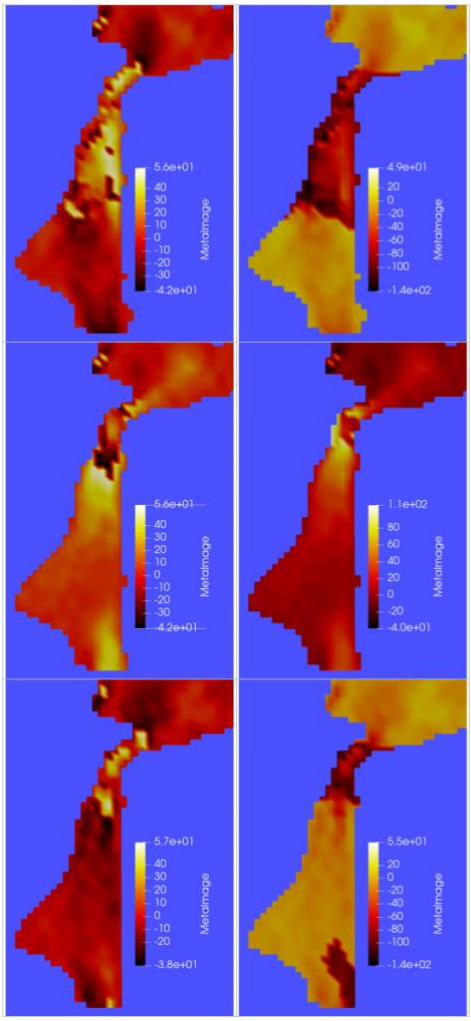

Figure 21: The velocity maps before correction of aliasing artifacts and after correction.

The first column represents raw data, and the second column represents corrected data.

Each line belongs to the different time phases of the same case.

4.4.3 Automated Correction of Partial Volume Artifacts and Flow Rate Calculation

Partial volume artifacts were corrected based on previous studies[50,66]. Only the aqueduct cerebri region was corrected because flow rate calculations are made in this region. The correction was made based on the following steps:

1. Aquaeductus cerebri were separated into two zones like in the previous research[50]. However, this step was not manually processed and was performed depending on the voxel positions based on the following criteria.
2. The voxels which are at the border were accepted as a region under partial artifact risks and named with zone-out (Z_{out}) (Figure 22).
3. The voxels that were not at the border were searched and these voxels were accepted as zone-in (Z_{in}) (Figure 22).

In the aqueducts stages which have zone-in, zone-out voxels' flows were calculated based on zone-in spatial average geometry magnitude. The flow rate calculation:

$$q(t) = \sum_{r \in aquaduct} q_r(t) \tag{23}$$

were updated depending on partial volume artifacts. For the correction, the equation in previous research needed an updating because tissues' magnitudes were in different distributions than in the previous study [50]. The following equation was applied for the correction of partial volume artifacts in this study:

$$q(t) = \sum_{r \in Z_{in}} q_r(t) + \sum_{r \in Z_{out}} \frac{m_r}{m_{in}} q_r \quad . \tag{24}$$

m_{in} could be calculated with:

$$m_{in} = \frac{1}{N_{in}} \sum_{r \in Z_{in}} m_r \tag{25}$$

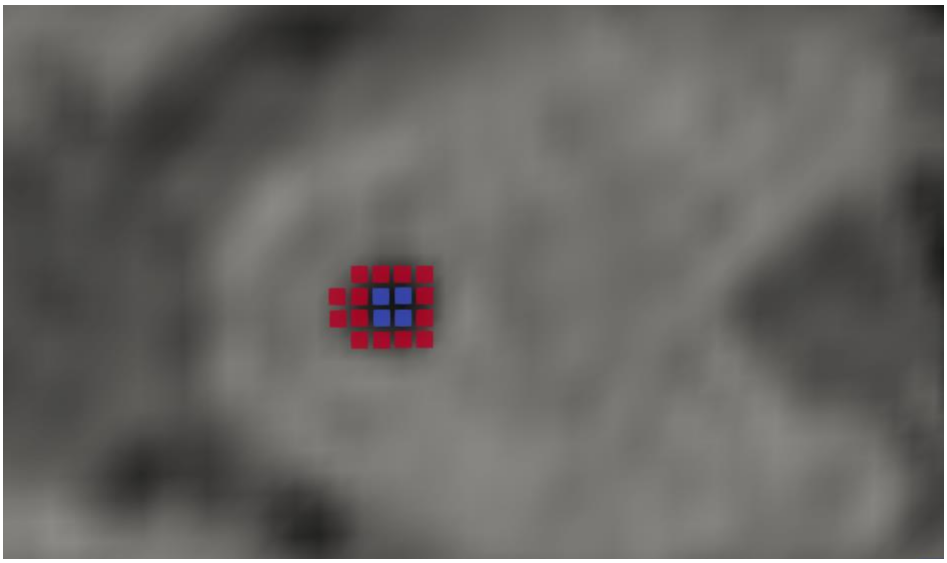

Figure 22: The representation of aqueducts cerebri voxels which were separated into zone-in and zone-out. Red voxels belong to the zone-out which includes voxels under suspect of the partial volume artifact, and blue voxels belong to the zone-in based on their locations.

4.5 Results

Aliasing artifacts were not detected in healthy cases' aqueducts cerebri. In 9 iNPH patients, 4 patients' data were corrected from aliasing artifacts during flow rate calculations. Figure 23 shows flow rates throughout aqueducts cerebri in each time phase before and after aliasing and partial volume artifacts corrections of the representative case. In the first three phases of this case even flow directions were obtained differently after the correction of aliasing artifacts, and the correction of partial volume artifacts nearly made %50 change in flowrates for this case.

Table 2 shows relative standard deviations of flow rates throughout aqueducts cerebri for evaluation of flow continuity in and correction methods reliability. Since velocity magnitudes were increased while correction of aliasing artifacts, relative standard deviations were calculated for comparison. In Case 4 relative standard deviations were found close to zero in 6-time phases than not-corrected data. Especially in the first phase relative standard deviation was decreased from 6 to 0.1 at Case 4. For Case 3 while some time phases are not showing a significant difference, the dramatic correction could be seen in the 7th and 8th-time phases.

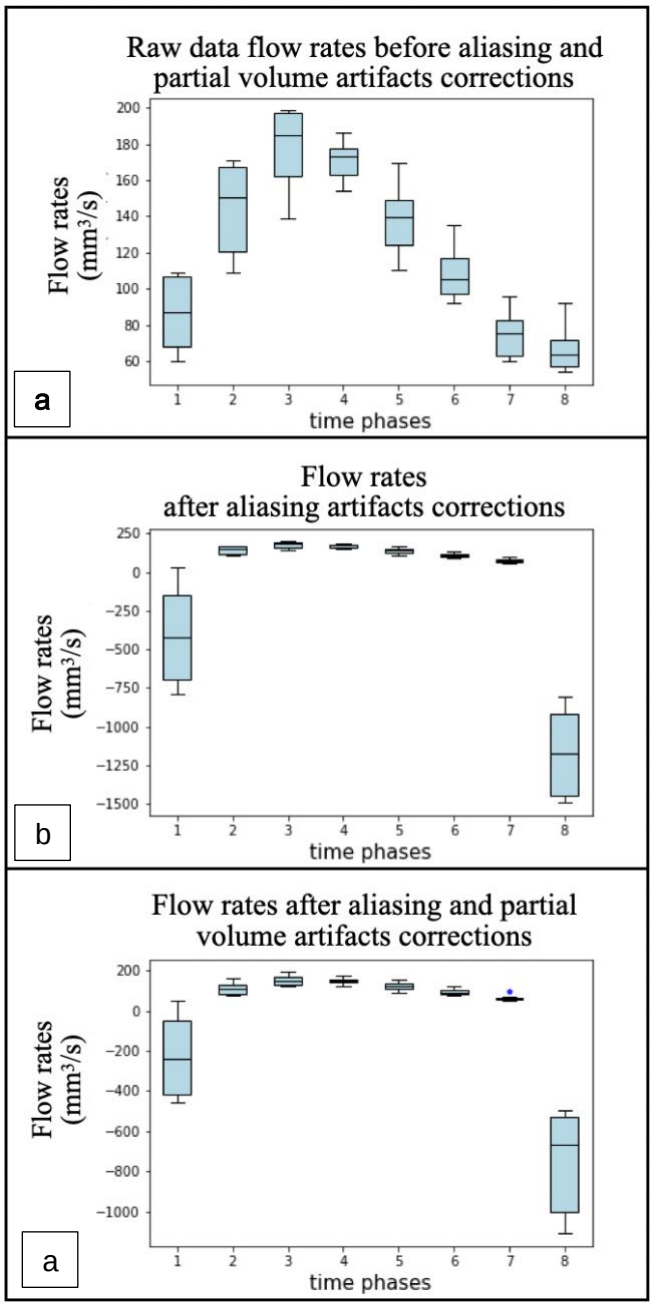

Figure 23: The representative case flow rates were calculated with raw data (a) and calculated after artifacts' corrections (b, c).

Table 2: The table shows relative standard deviations of flow rates which are obtained throughout aqueducts cerebri for each phase from 4 different cases. The columns with the “raw” title show relative standard deviations before any correction and the columns with the “corrected” title shows relative standard deviations after aliasing and partial volume artifacts’ corrections.

	Relative Standard Deviations of Flow Rates Throughout Aqueductus Cerebri							
	case 1		case 2		case 3		case 4	
	raw	corrected	raw	corrected	raw	corrected	raw	corrected
phase 1	0.346	0.262	0.245	0.902	0.067	0.204	6.091	0.143
phase 2	0.225	0.298	0.176	0.265	0.030	0.293	0.502	0.110
phase 3	0.847	3.791	0.127	0.176	0.193	0.124	1.488	0.612
phase 4	0.080	0.114	0.065	0.110	0.047	0.006	0.144	0.147
phase 5	0.152	0.205	0.141	0.179	0.090	0.009	0.261	0.088
phase 6	0.128	0.144	0.136	0.166	0.115	0.057	0.303	0.122
phase 7	0.136	0.159	0.172	0.243	1.017	0.052	0.734	0.803
phase 8	0.284	0.271	0.196	0.338	0.861	0.051	1.800	0.399

The comparison between iNPH patients and healthy cases for peak systolic (superior-inferior) and diastolic (inferior-superior) flow rates were shown in Figure 24. Significant differences were found in peak diastolic flow rates between iNPH patients and healthy subjects (p=0.022, Mann-Whitney's U test).

Aquaductus cerebri areas were also analyzed (Figure 25). For the comparison, average areas were calculated by using each stage area of aquaeductus cerebri throughout the selected aqueduct volume (Figure 17c). A significant difference between iNPH patients and healthy subjects was found (p=0.01, Mann-Whitney's U test).

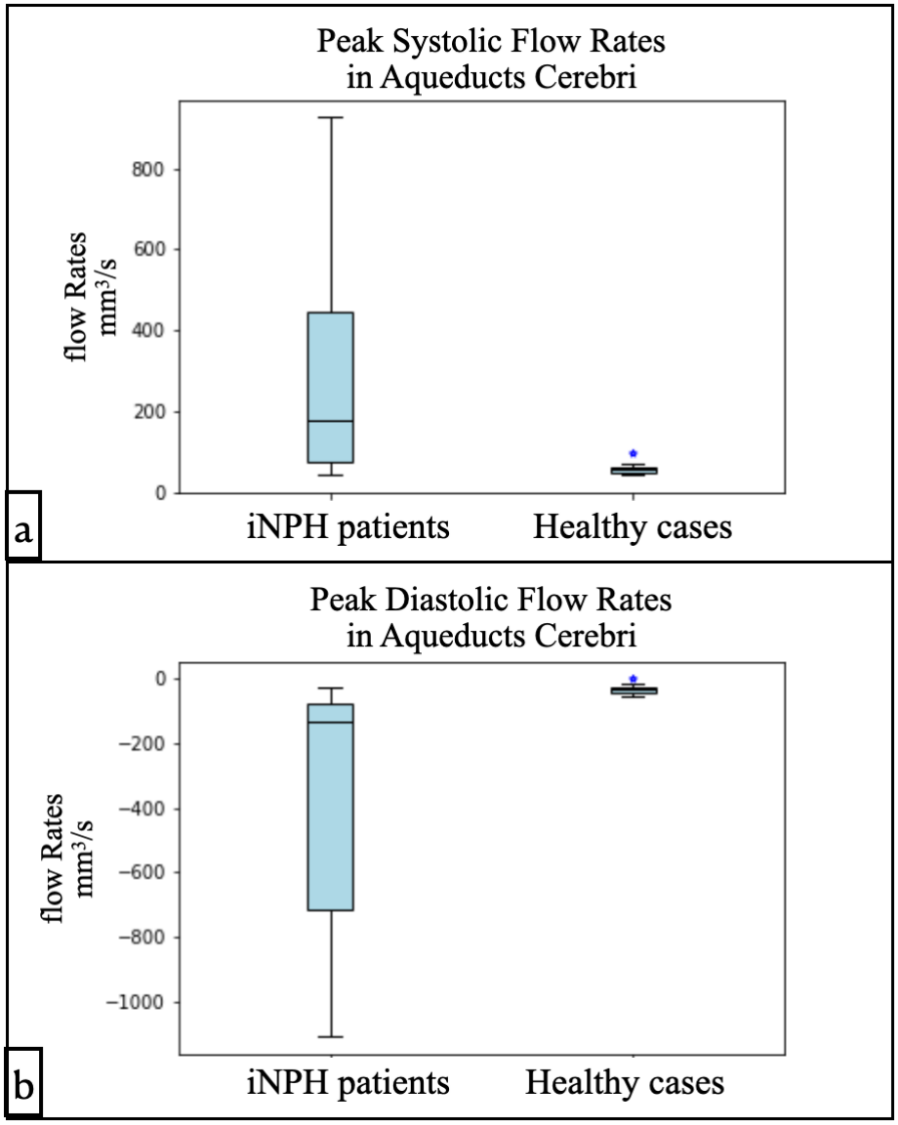

Figure 24: Peak flow rates' visualization of cases. 24a: Peak systolic flow rates of healthy cases and iNPH patients. 24b: Peak diastolic flow rates of healthy cases and iNPH patients.

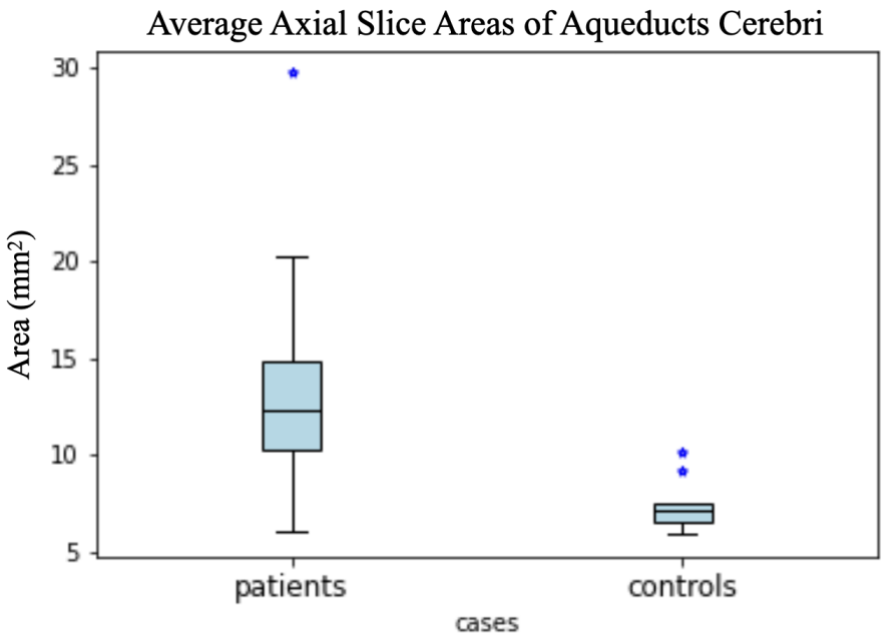

Figure 25: Average areas' of iNPH patients and healthy cases throughout aqueducts cerebri.

4.6 Discussion

In this chapter, objective calculation and correction approaches were suggested for the CSF flow throughout aqueduct cerebri. During the calculation process, VOI was chosen semiautomatically, and aliasing and partial volume artifacts were corrected automatically.

This chapter was presented as an alternative approach to 2D and manual CSF flow parameter calculation approaches[28,29,67,68], as the mostly automatically analyzing CSF flow in aqueducts as 3D. The automatic calculation approaches have been tried to build also in the previous studies by choosing aqueducts cerebri with segmentation methods like application threshold, or seed point[29]. Additionally, some studies investigated CSF flow parameters at different levels of aquaeductus cerebri and the importance of researcher-dependency[27,68]. Even though these studies investigated image processing dependencies with the aim of understanding the lack of consensus on using PC-MRI in clinical science at CSF flow analysis, still the common approach could not be built for the calculating process of flow parameters. At this point, in this chapter, possible automated calculation methods were shown which are made manually in

previous studies for improving and objectifying the calculation process of CSF flow parameters.

In this chapter, a 3D approach was suggested for the evaluation of flow in aqueducts cerebri by considering aqueducts cerebri's 3D structure which is not always straight and perpendicular to the axial plane. After obtaining VOI for the calculation, automated approaches were presented for the correction of aliasing and partial volume artifact corrections. These correction approaches were designed depending on previous studies' correction rules[28,50]. However, for finding aliased voxels automatically, the additional process developed by inspiring from previous automatic correction studies on blood flow imaging[59].

Examination of CSF flow as 3D showed a possibility of wrong corrections of aliasing artifacts considering only 2D data (Figure 13). Especially, for the representative case in Figure 23, for the first, second, and third phases, flow rates were seen as positive way and it could lead to wrong assumptions when evaluating with only 2D approaches. Consequently, it could be said that analyzing only 2D data could lead to unexpectedly

wrong results and evaluation of CSF flow in 3D is necessary for achieving correct and robust results.

The limitations of this study were analyzing data that have the same velocity encoding. Additionally, the number of cases was not adequate to building a parameter and evaluating the correction approach's ability. Depending on that, even though we found significant differences in peak diastolic flow rate and aqueduct area, the study is not competent for claiming generalization of these results.

However, in this study, the possibility of automated correction was shown with consideration of ventricle anatomy. We hope that this chapter could be an inspiration for further studies for improving completely objective flow calculation methods for the CSF analysis and more advanced studies could be managed without uncertainty.

5. Summary and Future Perspectives

In this research, 4D Flow MRI principles were explained in detail and their vital importance in CSF studies was pointed out. The limitations of using 4D flow MRI on CSF flow analysis were clarified. After the understanding of the relations between CSF flow analysis and limitations, phase offset correction methods were presented in Chapter 3. The suggested method includes a 3D correction of data automatically and provides objectivity in the process. Additionally, the method enables analysis of background noise and evaluation of the data quality. However, the data set was not enough for improving parameters within this study. In further studies, the parameters for the image quality could be improved. Furthermore, the main aim of this correction approach for the future, creating an environment for the visualization of CSF flow in 3D in any part of the ventricles.

In Chapter 4, the limitations of calculation flow parameters were mentioned. The segmentation approach for the ventricles was explained. However, the method was requiring manually marking stationary tissue around ventricles. Followingly, an approach for the correction of aliasing and partial volume artifacts was given. This chapter was prepared for presenting an example approach to possible automated correction and calculations to CSF

flow measurements. Anatomical-inspired aliasing correction approaches were explained. However, the correction method for the aliasing artifacts includes only the evaluation of neighbor voxels. Besides, this definition is only an estimation of the existence of aliasing artifacts. For making more robust corrections of aliasing artifacts, computational fluid dynamics also could be used additionally in further research.

Even though pointing to 3D flow analysis in this research, CSF was analyzed in only aqueducts cerebri because of the inappropriate velocity encoding for lateral ventricles and the third ventricle. However, we provided an approach for analyzing ventricles in 3D for further studies.

I hope that this study could be an inspiration for the integration of anatomical knowledge and computational studies and by using computational fluid dynamics more correct results could be obtained in future studies. With large data sets, automatic segmentation of ventricles also could be improved by further studies, and from the acquisition, parameter results of CSF could be obtained automatically, and subjectivity could be removed. In this way, we hope that large studies could be handled, and CSF pathophysiology could be understood more precisely in the future.

6. Bibliography

1. Moody DM. The blood-brain barrier and blood-cerebral spinal fluid barrier. In: *Seminars in Cardiothoracic and Vascular Anesthesia*. Vol 10. ; 2006:128-131. doi:10.1177/1089253206288992

2. Sakka L, Coll G, Chazal J. Anatomy and physiology of cerebrospinal fluid. *European Annals of Otorhinolaryngology, Head and Neck Diseases*. 2011;128(6):309-316. doi:10.1016/j.anorl.2011.03.002

3. Orešković D, Klarica M. The formation of cerebrospinal fluid: Nearly a hundred years of interpretations and misinterpretations. *Brain Research Reviews*. 2010;64(2):241-262. doi:10.1016/j.brainresrev.2010.04.006

4. Matsumae M, Sato O, Hirayama A, et al. Research into the physiology of cerebrospinal fluid reaches a new horizon: Intimate exchange between cerebrospinal fluid and interstitial fluid may contribute to maintenance of homeostasis in the central nervous system. *Neurologia Medico-Chirurgica*. 2016;56(7):416-441. doi:10.2176/nmc.ra.2016-0020

5. Orešković D, Radoš M, Klarica M. Role of choroid plexus in cerebrospinal fluid hydrodynamics. *Neuroscience*. 2017;354:69-87. doi:10.1016/j.neuroscience. 2017.04.025

6. Buishas J, Gould IG, Linninger AA. A computational model of cerebrospinal fluid production and reabsorption driven by Starling forces. *Croatian Medical Journal*. 2014;55(5):481-497. doi:10.3325/cmj.2014.55.481

7. Shen MD. Cerebrospinal fluid and the early brain development of autism. *Journal of Neurodevelopmental Disorders*. 2018;10(1). doi:10.1186/s11689-018-9256-7

8. Silverberg GD, Mayo M, Saul T, Rubenstein E, McGuire D. Alzheimer's disease, normal-pressure hydrocephalus, and senescent changes in CSF circulatory physiology: A hypothesis. *Lancet Neurology*. 2003;2(8):506-511. doi:10.1016/S1474-4422(03)00487-3

9. Yiallourou TI, Kröger JR, Stergiopulos N, Maintz D, Martin BA, Bunck AC. Comparison of 4D Phase-Contrast MRI Flow Measurements to Computational Fluid Dynamics Simulations of Cerebrospinal Fluid Motion in the Cervical Spine. *PLoS ONE*. 2012;7(12). doi:10.1371/journal.pone.0052284

10. Gholampour S, Fatouraee N. Boundary conditions investigation to improve computer simulation of cerebrospinal fluid dynamics in hydrocephalus patients. *Communications Biology*. 2021;4(1). doi:10.1038/s42003-021-01920-w

11. Mantovani G, Menegatti M, Scerrati A, Cavallo MA, de Bonis P. Controversies and Misconceptions Related to Cerebrospinal Fluid Circulation: A Review of the Literature from the Historical Pioneers' Theories to Current Models. *BioMed Research International*. 2018;2018. doi:10.1155/2018/2928378

12. Bulat M, Klarica M. Recent insights into a new hydrodynamics of the cerebrospinal fluid. *Brain Research Reviews*. 2011;65(2):99-112. doi:10.1016/j.brainresrev. 2010.08.002

13. Brinker T, Stopa E, Morrison J, Klinge P. A new look at cerebrospinal fluid circulation. *Fluids and Barriers of the CNS*. 2014;11(1). doi:10.1186/2045-8118-11-10

14. Orešković, Darko, Marijan Klarica, and Miroslav Vukić. "The formation and circulation of cerebrospinal fluid inside the cat brain ventricles: a fact or an illusion?." Neuroscience letters 327, no. 2 (2002): 103-106.

15. Klarica M, Orešković D, Božić B, Vukić M, Butković V, Bulat M. New experimental model of acute aqueductal blockage in cats: Effects on cerebrospinal fluid pressure and the size of brain ventricles. *Neuroscience*. 2009;158(4):1397-1405. doi:10.1016/j.neuroscience.2008.11.041

16. Miyajima M, Arai H. Evaluation of the production and absorption of cerebrospinal fluid. *Neurologia Medico-Chirurgica*. 2015;55(8):647-656. doi:10.2176/nmc.ra.2015-0003

17. Langham MC, Jain V, Magland JF, Wehrli FW. Time-resolved absolute velocity quantification with projections. *Magnetic Resonance in Medicine*. 2010;64(6):1599-1606. doi:10.1002/mrm.22559

18. Kowallick JT, Joseph AA, Unterberg-Buchwald C, et al. Real-time phase-contrast flow MRI of the ascending aorta and superior vena cava as a function of intrathoracic pressure (Valsalva manoeuvre). *British Journal of Radiology*. 2014;87(1042). doi:10.1259/bjr.20140401

19. Sträter A, Huber A, Rudolph J, et al. 4D-Flow MRI: Technique and Applications. *RoFo Fortschritte auf dem Gebiet der Rontgenstrahlen und der Bildgebenden Verfahren*. 2018;190(11):1025-1035. doi:10.1055/a-0647-2021

20. Pelc NJ, Herfkens RJ, Enzmann DR. *Phase Contrast Cine Magnetic Resonance Imaging Instrumentation of 3D Micro Nano-CT with Submicron Resolution View Project Compression for Medical Imaging View Project*.; 1991.

21. Chinchali, Avinash Pramod. Eddy current correction in PC-MRI: an analysis of local and global static tissue fitting techniques. *University of California, Los Angeles, 2018.*

22. Spees WM, Buhl N, Sun P, Ackerman JJH, Neil JJ, Garbow JR. Quantification and compensation of eddy-current-induced magnetic-field gradients. *Journal of Magnetic Resonance*. 2011;212(1):116-123. doi:10.1016/j.jmr.2011.06.016

23. Giese D, Haeberlin M, Barmet C, Pruessmann KP, Schaeffter T, Kozerke S. Analysis and correction of background velocity offsets in phase-contrast flow measurements using magnetic field monitoring. *Magnetic Resonance in Medicine*. 2012;67(5):1294-1302. doi:10.1002/mrm.23111

24. Lorenz R, Bock J, Snyder J, Korvink JG, Jung BA, Markl M. Influence of eddy current, Maxwell and gradient field corrections on 3D flow visualization of 3D CINE PC-MRI data. *Magnetic Resonance in Medicine*. 2014;72(1):33-40. doi:10.1002/mrm.24885

25. Nayak KS, Nielsen JF, Bernstein MA, et al. Cardiovascular magnetic resonance phase contrast imaging. *Journal of Cardiovascular Magnetic Resonance*. 2015;17(1). doi:10.1186/s12968-015-0172-7

26. Luetmer, Patrick H., John Huston, Jonathan A. Friedman, Geoffrey R. Dixon, Ronald C. Petersen, Clifford R. Jack, Robyn L. McClelland, and Michael J. Ebersold. "Measurement of cerebrospinal fluid flow at the cerebral aqueduct by use of phase-contrast magnetic resonance imaging: technique validation and utility in diagnosing idiopathic normal pressure hydrocephalus." *Neurosurgery 50, no. 3 (2002): 534-543.*

27. Lee, Jeong Hyun, Ho Kyu Lee, Jae Kyun Kim, Hyun Jeong Kim, Ji Kang Park, and Choong Gon Choi. "CSF flow quantification of the cerebral aqueduct in normal volunteers using phase contrast cine MR imaging." *Korean journal of radiology 5, no. 2 (2004): 81-86.*

28. Lindstrøm EK, Ringstad G, Mardal KA, Eide PK. Cerebrospinal fluid volumetric net flow rate and direction in idiopathic normal pressure hydrocephalus. *NeuroImage: Clinical*. 2018;20:731-741. doi:10.1016/j.nicl.2018.09.006

29. Forner Giner J, Sanz-Requena R, Flórez N, et al. Quantitative phase-contrast MRI study of cerebrospinal fluid flow: a method for identifying patients with normal-pressure hydrocephalus. *Neurología (English Edition)*. 2014;29(2):68-75. doi:10.1016/j.nrleng.2013.12.006

30. Miskin N, Patel H, Franceschi AM, et al. Diagnosis of normal-pressure hydrocephalus: Use of traditional measures in the era of volumetric MR imaging. *Radiology*. 2017;285(1):197-205. doi:10.1148/radiol.2017161216

31. Shanks J, Markenroth Bloch K, Laurell K, et al. Aqueductal CSF stroke volume is increased in patients with idiopathic normal pressure hydrocephalus and decreases after shunt surgery. *American Journal of Neuroradiology*. 2019;40(3):453-459. doi:10.3174/ajnr.A5972

32. Flórez YN, Moratal D, Forner J, et al. Semiautomatic analysis of phase contrast magnetic resonance imaging of cerebrospinal fluid flow through the aqueduct of Sylvius. *Magnetic Resonance Materials in Physics, Biology and Medicine*. 2006;19(2):78-87. doi:10.1007/s10334-006-0030-6

33. Vassiliou VS, Cameron D, Prasad SK, Gatehouse PD. Magnetic resonance imaging: Physics basics for the cardiologist. *JRSM Cardiovascular Disease*. 2018;7:204800401877223. doi:10.1177/2048004018772237

34. Nayler, G. L., D. N. Firmin, and D. B. Longmore. "Blood flow imaging by cine magnetic resonance." J Comput Assist Tomogr 10, no. 5 (1986): 715-722.

35. Pooley RA. Fundamental physics of MR imaging. *Radiographics*. 2005;25(4):1087-1099. doi:10.1148/rg.254055027

36. Rosen BR, Brady TJ. Principles of nuclear magnetic resonance for medical application. *Seminars in Nuclear Medicine*. 1983;13(4):308-318. doi:10.1016/S0001-2998(83)80043-9

37. Mlynárik V. Introduction to nuclear magnetic resonance. *Analytical Biochemistry*. 2017;529:4-9. doi:10.1016/j.ab.2016.05.006

38. Bloch F. *NUCLEAR MAGNETISM*. Vol 43. American Scientist; 1955.

39. Packard, F. Bloch WW Hansen M. "The nuclear induction experiment." Physical Review 70, no. 7-8 (1946): 474-485.

40. Chavhan GB, Babyn PS, Thomas B, Shroff MM, Mark Haacke E. Principles, techniques, and applications of T2*-based MR imaging and its special applications. *Radiographics*. 2009;29(5):1433-1449. doi:10.1148/rg.295095034

41. Hajidah DH, Dwihapsari Y. Quantitative T2magnetic resonance imaging: Analysis of the effect of echo time on images and signal to noise ratio on agarose. In: *AIP Conference Proceedings*. Vol 2346. American Institute of Physics Inc.; 2021. doi:10.1063/5.0048234

42. Sprawls, Perry. Magnetic resonance imaging: principles, methods, and techniques. Madison: Medical Physics Publishing, 2000.

43. Korbecki A, Zimny A, Podgórski P, Sąsiadek M, Bladowska J. Imaging of cerebrospinal fluid flow: Fundamentals, techniques, and clinical applications of phase-contrast magnetic resonance imaging. *Polish Journal of Radiology*. 2019;84:240-250. doi:10.5114/pjr.2019.86881

44. Wymer DT, Patel KP, Burke WF, Bhatia VK. Phase-contrast MRI: Physics, techniques, and clinical applications. *Radiographics*. 2020;40(1):122-140. doi:10.1148/rg.2020190039

45. Stankovic, Zoran, Bradley D. Allen, Julio Garcia, Kelly B. Jarvis, and Michael Markl. "4D flow imaging with MRI." Cardiovascular diagnosis and therapy 4, no. 2 (2014): 173.

46. Azarine A, Garçon P, Stansal A, et al. Four-dimensional Flow MRI: Principles and Cardiovascular Applications. *Radiographics*. 2019;39(3):632-648. doi:10.1148/rg.2019180091

47. Lankhaar JW, Hofman MBM, Marcus JT, Zwanenburg JJM, Faes TJC, Vonk-Noordegraaf A. Correction of phase offset errors in main pulmonary artery flow quantification. *Journal of Magnetic Resonance Imaging*. 2005;22(1):73-79. doi:10.1002/jmri.20361

48. Erasmus, L. J., D. Hurter, M. Naudé, H. G. Kritzinger, and S. Acho. "A short overview of MRI artefacts." SA Journal of Radiology 8, no. 2 (2004).

49. Shurche S, Riyahi-Alam N. *Evaluation of Geometric Distortion Artifacts in Structural Magnetic Resonance Imaging*. Vol 4.; 2017.

50. Bouillot P, Delattre BMA, Brina O, et al. 3D phase contrast MRI: Partial volume correction for robust blood flow quantification in small intracranial vessels. *Magnetic Resonance in Medicine*. 2018;79(1):129-140. doi:10.1002/mrm.26637

51. Bernstein MA, Zhou XJ, Polzin JA, et al. Concomitant gradient terms in phase contrast MR: Analysis and correction. *Magnetic Resonance in Medicine*. 1998;39(2):300-308. doi:10.1002/mrm.1910390218

52. Gatehouse PD, Rolf MP, Bloch KM, et al. A multi-center inter-manufacturer study of the temporal stability of phase-contrast velocity mapping background offset errors. *Journal of Cardiovascular Magnetic Resonance*. 2012;14(1). doi:10.1186/1532-429X-14-72

53. Spijkerman JM, Geurts LJ, Siero JCW, Hendrikse J, Luijten PR, Zwanenburg JJM. Phase contrast MRI measurements of net cerebrospinal fluid flow through the cerebral aqueduct are confounded by respiration. *Journal of Magnetic Resonance Imaging*. 2019;49(2):433-444. doi:10.1002/jmri.26181

54. Ahmad N, Salama D, Al-Haggar M. MRI CSF flowmetry in evaluation of different neurological diseases. *Egyptian Journal of Radiology and Nuclear Medicine*. 2021;52(1). doi:10.1186/s43055-021-00429-w

55. Xu Q, Yu SB, Zheng N, et al. Head movement, an important contributor to human cerebrospinal fluid circulation. *Scientific Reports*. 2016;6. doi:10.1038/srep31787

56. Elsafty H, ELAggan A, Yousef M, Badawy M. Cerebrospinal fluid flowmetry using phase-contrast MRI technique and its clinical applications. *Tanta Medical Journal*. 2018;46(2):121. doi:10.4103/tmj.tmj_55_17

57. Zahid AM, Martin B, Collins S, Oshinski JN, Ethier CR. Quantification of arterial, venous, and cerebrospinal fluid flow dynamics by magnetic resonance imaging under simulated micro-gravity conditions: a prospective cohort study. *Fluids and Barriers of the CNS*. 2021;18(1). doi:10.1186/s12987-021-00238-3

58. Dunås T, Holmgren M, Wåhlin A, Malm J, Eklund A. Accuracy of blood flow assessment in cerebral arteries with 4D flow MRI: Evaluation with three segmentation methods. *Journal of Magnetic Resonance Imaging*. 2019;50(2):511-518. doi:10.1002/jmri.26641

59. Muth S, Dort S, Sebag IA, Blais MJ, Garcia D. Unsupervised dealiasing and denoising of color-Doppler data. *Medical Image Analysis*. 2011;15(4):577-588. doi:10.1016/j.media.2011.03.003

60. Solem JE, Persson M, Heyden A. Velocity based segmentation in phase contrast MRI images. In: *Lecture Notes in Computer Science*. Vol 3216. Springer Verlag; 2004:459-466. doi:10.1007/978-3-540-30135-6_56

61. Van Pelt R, Nguyen H, ter Haar Romeny B, Vilanova A. Automated segmentation of blood-flow regions in large thoracic arteries using 3D-cine PC-MRI measurements. *International Journal of Computer Assisted Radiology and Surgery*. 2012;7(2):217-224. doi:10.1007/s11548-011-0642-9

62. Khan MA, Liu J, Tarumi T, et al. Measurement of cerebral blood flow using phase contrast magnetic resonance imaging and duplex ultrasonography. *Journal of Cerebral Blood Flow and Metabolism*. 2017;37(2):541-549. doi:10.1177/0271678X16631149

63. Srichai MB, Lim RP, Wong S, Lee VS. Cardiovascular applications of phase-contrast MRI. *American Journal of Roentgenology*. 2009;192(3):662-675. doi:10.2214/AJR.07.3744

64. Metwali A, Ahmed H, Abdalsamie HA, Sayed M, Elshandawely. Role of MRI CSF flowmetry in differantiation between normal pressure hydrocephalus and invoultional brain changes. I. International Journal of Multidisciplinary Research and Development. 2021;8(12):106-113.

65. Nahas H, Au JS, Ishii T, Yiu BYS, Chee AJY, Yu ACH. A Deep Learning Approach to Resolve Aliasing Artifacts in Ultrasound Color Flow Imaging. *IEEE Transactions on Ultrasonics, Ferroelectrics, and Frequency Control*. 2020;67(12):2615-2628. doi:10.1109/TUFFC.2020.3001523

66. Tang, Chao, Duane D. Blatter, and Dennis L. Parker. "Correction of partial-volume effects in phase-contrast flow measurements." Journal of Magnetic Resonance Imaging 5, no. 2 (1995): 175-180.

67. Scollato A, Tenenbaum R, Bahl G, Celerini M, Salani B, di Lorenzo N. Changes in aqueductal CSF stroke volume and progression of symptoms in patients with unshunted idiopathic normal pressure hydrocephalus. *American Journal of Neuroradiology*. 2008;29(1):192-197. doi:10.3174/ajnr.A0785

68. Tawfik AM, Elsorogy L, Abdelghaffar R, Naby AA, Elmenshawi I. Phase-contrast MRI CSF flow measurements for the diagnosis of normal-pressure hydrocephalus: Observer agreement of velocity versus volume parameters. *American Journal of Roentgenology*. 2017;208(4):838-843. doi:10.2214/AJR.16.16995

Publication List

(i) Original papers

1- Yavuz Ilik, Selin, Tomohiro Otani, Shigeki Yamada, Yoshiyuki Watanabe, and Shigeo Wada. "A subject-specific assessment of measurement errors and their correction in cerebrospinal fluid velocity maps using 4D flow MRI." Magnetic Resonance in Medicine 87, no. 5 (2022): 2412-2423.

2- Tomohiro Otani, Hiroshi Yamashita, Kazuma Iwata, Selin Yavuz Ilik, Shigeki Yamada, Yoshiyuki Watanabe, and Shigeo Wada. "A concept on velocity estimation from magnetic resonance velocity images based on variational optimal boundary control." Journal of Biomechanical Science and Engineering (2022): 22-00050.

(ii) Conferences

Yavuz Ilik, Selin, Tomohiro Otani, Shigeki Yamada, Yoshiyuki Watanabe, and Shigeo Wada. “Correction of eddy-current based phase offset errors in cerebrospinal fluid flow measurement: four-dimensional flow magnetic resonance imaging” Asian Biomechanics Conference, December 2021.

Acknowledgments

First, I would like to thank Prof. Shigeo Wada (supervisor) for accepting me as his student and for his kindness, prudence, and wisdom. I could not imagine success in this pathway without Wada sensei. I would like to thank Assoc Prof. Tomohiro Otani for his advice and support during this journey. I am grateful for his patience and encouragement during my learning process. I can't thank them enough for the taught me to look from different perspectives.

This work was supported by the Japan Society for the Promotion of Science Grants-in-Aid for Scientific Research (19H01175 and 21K18037).

I present my sincere greatness to the Ministry of Education, Culture, Sports, Science, and Technology for supporting me with a scholarship.

I present my appreciation to Prof. Yoshiyuki Watanabe and Dr. Shigeki Yamada for their collaborations during research.

I would like to thank each person in the Graduate Student Section of the Graduate School of Engineering Sciences for their support and kindness. Especially, I am so grateful to Hiromi Ishikawa and Hanako Nakajima for their kindness and understanding.

I am grateful to Prof. Osamu Oshiro and Prof. Shinji Deguchi for their review and precious suggestions for this thesis.

I express gratitude to Prof. Dr. M. Özgur Taskapilioglu and Prof. Dr. Esra Kunt Uzaslan for always making me feel their support.

I want to thank my family. To my little sister and my brother for making me a big sister and they gave me energy for work and hope for a better world. I can’t thank you enough, my mother, who brought me into the world, and I am grateful to my mother and father for always believing in me.

Lastly, I would like to thank my husband for being the most understandable and supportive husband in the world. I am so grateful to him understand me and supporting my decisions at all costs.

Most importantly, I would like to thank God for always helping and guiding me at the deepest and happiest moments, and for making me focus on my research.